

Efficiency of Parallel Transmission Methods at 7T Magnetic Resonance

Dissertation

zur Erlangung des akademischen Grades

doctor rerum naturalium

(Dr. rer. nat.)

genehmigt durch die Fakultät für Naturwissenschaften

der Otto-von-Guericke-Universität Magdeburg

von **M. Sc. Niravkumar Darji**

geb. am 06.04.1984 in Sidhpur, India

Gutachter: **Prof. Dr. rer. nat. habil. Oliver Speck**

Gutachter: **Prof. Dr. Harald Möller**

eingereicht am: 10.06.2014

verteidigt am: 06.11.2014

To my parents, my wife and my daughter (Delsy)

Table of Contents

Table of Contents	i
List of Figures	iii
Abstract	v
Zusammenfassung.....	vii
Acknowledgements.....	ix
Glossary.....	x
1. Introduction.....	1
1.1. Motivation	1
1.2. Aims and objectives of this Ph.D. Dissertation	4
2. Background	6
2.1. Magnetic Resonance Imaging.....	6
2.2. RF excitation	9
2.2.1. Basic excitation principles.....	10
2.2.2. Excitation methods in MR	17
2.3. RF shimming	21
2.3.1. Static RF shimming.....	22
2.3.2. Transmit-SENSE	23
3. Materials and Methods	28
3.1. Experimental Setup.....	28
3.2. B_1^+ mapping.....	34
3.3. RF shimming	37
3.3.1. Static RF shimming.....	37
3.3.2. pTx spokes RF waveforms	39
3.4. RF shim approach.....	41
3.4.1. Global and slice-selective RF shimming.....	42
3.4.2. RF-shimming on higher number of Tx channel	43

3.5.	RF shim setting implementation.....	45
3.6.	Imaging sequence protocol.....	46
4.	Results	48
4.1.	Global and slice-selective RF shimming.....	48
4.2.	Higher number of Tx channels	55
4.3.	Quantitative studies	60
5.	Discussion	68
6.	Conclusion.....	74
	References	75
	Publications.....	81
	Erklärung	82

List of Figures

Figure 1: K-space trajectory considered for pTx applications.....	26
Figure 2: Schematic representation of the parallel transmission hardware	30
Figure 3: Voxel model & SAR simulation of body coil.....	32
Figure 4: Sequence diagram of B_1^+ mapping saturated TFL sequence.....	35
Figure 5: B_1^+ map of individual Tx channel.....	37
Figure 6: K-space trajectories of 2- and 3- spokes RF pulses	40
Figure 7: Configurations of various combinations of Tx channels	44
Figure 8: Comparison of CP and RF shimmed B_1^+ maps acquired in transversal and sagittal orientations	49
Figure 9: Comparison of CP and RF shimmed anatomical images acquired in transversal and sagittal orientations.....	50
Figure 10: Global and slice selective RF shimmed B_1^+ maps of transversal oriented slice stack.....	52
Figure 11: Global and slice selective RF shimmed B_1^+ maps of sagittal oriented slice stack.....	53
Figure 12: Global and slice selective RF shimmed GRE images of sagittal oriented slice stack.....	55
Figure 13: RF shimming on higher number of Tx channel for single slice.	57
Figure 14: RF shimming on higher number of Tx channel for multi slice.	59

Figure 15: Comparing slice-selective RF shimming and global RF shimming methods, and higher number of Tx channels..... 61

Figure 16: Changes in RF-power and RMMSE of B_1^+ with slice locations..... 65

Figure 17: Tradeoffs between relative RF-power and RMMSE for 1-, 2-, 4-, and 8-channel Tx configurations for slice-selective and global RF shimming methods..... 67

Abstract

Magnetic Resonance Imaging plays a vital role in visualizing the structure and function of the human body. In recent years, ultra-high magnetic field has emerged as an attractive means to achieve significant improvements in both signal-to-noise ratio and image contrast. However, during *in vivo* imaging at ultra-high fields the dielectric resonance effects and radio-frequency power deposition have become challenging issues for magnetic resonance imaging.

This work addresses the challenges mentioned above by developing method using parallel transmit system. Here, an 8-channel transmit receive head coil array was used, along with emulated circular polarized system and 2-, 4-, and 8-channel independent transmit configurations at 7T. Static RF shimming and spokes pulses were employed on human subjects in order to homogenize the B_1^+ field in the excited volume. Initially the effect on B_1^+ homogeneity and radio-frequency power were scrutinized by applying radio frequency shimming on circular polarized mode and 2-, 4-, and 8-channel transmit configurations on multi-slice acquisition *in vivo* at 7T. In addition, slice-selective and global radio-frequency shimming methods were applied on circular polarized and 2-, 4-, and 8-channel transmit channel configurations to investigate the further improvement in B_1^+ homogeneity and radio frequency power.

Systematic improvement in B_1^+ homogeneity and/or reduction in radio-frequency power were observed when employing higher number of transmit channels with slice selective shimming. It was found that radio-frequency shimming in the human brain with 8-channel transmission and slice-selective shimming yields an increase in B_1^+ homogeneity and/or reduction in power by 25% and 45% for transversal and sagittal orientations respectively, when compared with circular polarized global shimming at 7T.

Zusammenfassung

Die Magnetresonanztomographie spielt eine wichtige Rolle bei der Visualisierung von Struktur und Funktion im menschlichen Körper. In den letzten Jahren haben sich ultrahohe Magnetfeld stärken als ein attraktives Mittel etabliert, um signifikante Verbesserungen sowohl im Signal-zu-Rausch-Verhältnis als auch beim Kontrast zu erzielen. Bei der Bildgebung mittels ultrahoher Magnetfelder stellten sich sowohl dielektrische Resonanzeffekte als auch SAR-Grenzwerte als fordernde Themen heraus. Die Verwendung von Sendespulenordnungen mit unabhängigen Hochfrequenzquellen über ein paralleles Übertragungssystem ist ein vielversprechendes Verfahren zur Verringerung der resultierenden B_1^+ -Inhomogenitäten.

Das Hauptziel der vorliegenden Arbeit ist es, die notwendigen Methoden zur Verwendung von parallelen Übertragungssystemen anstelle des Standard-Systems zu erarbeiten. Hierbei werden verschiedene robuste und zuverlässige Methoden unter Verwendung des Hochfrequenz-Shims mit parallelen Sendesystemen im Vergleich mit dem Standard-System untersucht.

Diese Arbeit befasst sich mit den oben genannten Herausforderungen, indem sowohl die B_1^+ -Inhomogenität als auch die Radiofrequenzleistung minimiert werden. Hierbei wurde eine 8-Kanal-Kopfspule als Sende-Array verwendet, neben emulierten, zirkular

polarisierten Sende-Konfigurationen mit zwei, vier und acht unabhängigen Kanälen. Statische RF-Shim- und Spokes-Pulse wurden *in vivo* angewandt, um das B_1^+ -Feld im angeregten Volumen zu homogenisieren. Im ersten Schritt wurde der Effekt auf B_1^+ -Inhomogenität und RF-Sendeleistung untersucht, indem RF-Shimming im zirkular polarisierten Modus und mittels 2-, 4- und 8-Kanal-Sendekonfigurationen auf Mehrschichtmessungen *in vivo* bei 7T angewandt wurde. Des Weiteren wurden schichtselektive und globale RF-Shimming-Methoden auf sowohl zirkular polarisierte als auch 2-, 4-, und 8-Kanal-Spulenkonfigurationen angewandt, um eine weitere Verbesserung sowohl der B_1^+ -Homogenität als auch der RF-Sendeleistung zu untersuchen.

Beim Einsatz einer steigenden Zahl an Sendekanälen und unter Verwendung von schichtselektivem Shim wurde eine fortlaufende Verbesserung der B_1^+ -Homogenität und/oder Verringerung der Hochfrequenzleistung beobachtet. Es wurde festgestellt, dass RF-Shimming im menschlichen Gehirn zu einer verbesserten B_1^+ -Homogenität und reduzierten Hochfrequenz-Sendeleistung von 25% bzw. 45% für transversale bzw. sagittale Schichten im Vergleich zu zirkular polarisiertem, globalen Shimming, führt.

Acknowledgements

I wish to express my thanks to the many people who have helped and inspired me during my doctoral studies.

I especially wish to express my sincere appreciation to my supervisor, Prof. Dr. Oliver Speck, director of the Department of Biomedical Magnetic Resonance (BMMR), Otto-von-Guericke University of Magdeburg, for his excellent guidance, caring, patience, friendship, and wisdom. He provided me with an excellent atmosphere, encouragement, inspiration, and motivation for doing research and enabled me to complete this research work smoothly and successfully.

In addition, I would like to thank Dr. Hans-peter Fautz for providing me training to start work on pTx system and providing me useful tools for my project. Thanks also to our BMMR team members for their valuable input in research and life through our interactions during the long hours in the lab. In particular, I would like to thank Weiqiang (Chris), who has been good friend from the start and made things run smoothly.

I am very grateful to my parents, elder sister, my family and parents in law. They were always supporting and encouraging me with their best wishes.

Last but not least, I am greatly indebted to my devoted wife Himali and my daughter Delsy. Their love and support without any complaints or regrets have allowed me complete this doctoral study.

Glossary

Abbreviation	Meaning
7T	7 Tesla
B_0	Static magnetic field
B_1^+	Transmit sensitivity
B_1^-	Receive sensitivity
BOLD	Blood oxygen level dependent
CNR	Contrast to noise ratio
CP	Circular polarized
FA	Flip angle
FOV	Field of view
FLASH	Fast low angle shot (sequence)
fMRI	Functional MRI
GRE	Gradient recalled echo (sequence)
MR	Magnetic resonance
MRI	Magnetic resonance imaging
pTx	Parallel transmission
ROI	region of interest
RF	Radio frequency
RMMSE	Root magnitude mean square error

SAR	Specific absorption rate
SE	Spin echo (sequence)
SENSE	Sensitivity encoding
SNR	Signal to noise ratio
T1w	T1 weighted
T2w	T2 weighted
TE	Time of echo
TFL	Turbo FLASH (sequence)
TR	Time of repetition
TSE	Turbo spin echo (sequence)
Tx	Transmit
UHF	Ultra high field (3-Tesla and up)

Introduction

1.1. Motivation

Magnetic resonance imaging (MRI) is a non-invasive and extremely valuable diagnostic imaging tool. MRI scans present medical professionals with an accurate and detailed image of the organs and tissues within the human body [1]. MRI uses magnetic fields and radio-waves to generate images, and is the preferred imaging method for diagnosing many soft-tissue disorders, especially those found in the brain [2–4], musculoskeletal [5], pelvis [6,7] and angiographic imaging [8,9].

Magnetic resonance imaging consists of two distinct phases or stages. The first phase is the excitation phase which involves generating a MR signal in the subject using a Radio Frequency (RF) pulse. The second phase is the acquisition phase during which the generated signal is manipulated and collected. These two steps are repeated sequentially several times in order to acquire enough data to create an image. This

INTRODUCTION

dissertation is concerned mainly with the excitation phase of MRI, and particularly with the methods of homogenizing RF field for ultra-high magnetic field MRI.

During the excitation phase, the RF excitation and subsequent signal generation are localized to specific regions within the subject, such as a three dimensional (3D) slab or a relatively thin two dimensional (2D) slice. In the subsequent acquisition phase, the 3D slab is encoded in all three dimensions, while the thin 2D slice is resolved only in-plane by the acquisition phase [10]. This localization of the RF excitation followed by the relevant signal manipulation produces a clinical image with the desired contrast, resolution, and field of view. To create such localized and uniform excitations, customized RF pulses are required. In typical commercial MRI scanners which operate at a main magnetic field strength, B_0 , of 1.5 Tesla (T) or lower, localized single-slice or slab-selective excitations are relatively simple, and are routinely employed in clinical imaging.

Recently, there is a greater interest in using higher magnetic field strength in MR imaging. Some of the benefits of high field MR systems include increased signal-to-noise ratio (SNR) [11–13], increased contrast-to-noise ratio (CNR) [14] and improved chemical selectivity [15,16]. There are several applications using higher field strength MRIs [17,18], such as functional MRI (fMRI), magnetic resonance angiography (MRA), and magnetic resonance spectroscopy (MRS). High magnetic fields have the most impact in fMRI applications due to the increased magnetic susceptibility, which enhances the blood oxygenation level dependent (BOLD) contrast [18–21].

INTRODUCTION

While there are a number of benefits associated with higher field MRI, the increased field strength also leads to many technical challenges. Higher field strength causes greater transmit RF field (B_1^+) inhomogeneity, thus increasing the amount of RF energy deposited in tissue, and leading to increased susceptibility artifacts [22–25]. The B_1^+ inhomogeneity of the circularly polarized (CP) RF field also creates variable tissue contrast depending on the geometry and the magnetic field strengths [26–28].

The B_1^+ inhomogeneity is a significant issue for high field MRI and will be addressed throughout this dissertation. The B_1^+ inhomogeneity causes an uneven distribution of signal intensity across an image. This effect can result in the loss of details in one or more particular areas of the image. In high field MRI, the lack of uniformity is more severe than in low field MRI since the B_1^+ field propagating through the object has shorter wavelengths and greater attenuation [29].

Various methods have been proposed for reducing B_1^+ inhomogeneity, Many of these methods are already implemented on current imaging systems, e.g., the use of composite pulses [30], 3D RF excitation [31,32] and adiabatic pulses [33]. Another approach is the use of multiple transmit channels [34–36], which can be implemented in combination with the previously mentioned methods [37]. This technique requires a substantial additional investment in hardware. The basic idea behind the multi-channel transmit concept is to geometrically break the transmit field into multiple regions, where each region is controlled independently, thus creating spatial degrees of freedom that allow the delivery of specific excitation pulses from individual transmit channels. The

INTRODUCTION

parallel transmit (pTx) hardware allows channel specific control over RF amplitudes and excitation phases that can mitigate high field B_1^+ inhomogeneity, either globally or for isolated target anatomy [38]. This concept is known as B_1^+ shimming, or static RF shimming [27,39–41].

Systematic previous studies on RF shimming have primarily examined two independent transmit channels [42], but nowadays RF shimming on eight or more independent transmit channels has been studied [43–48]. In an effort to increase the number of degrees of freedom available for such RF field shaping, there has been a trend towards the use of a larger number of transmit channels, thus mirroring the development of parallel reception architecture in the past decade [41,43,49–51].

1.2. Aims and objectives of this Ph.D. Dissertation

As mentioned previously, RF shimming using parallel transmit hardware plays an important role in reducing the B_1^+ inhomogeneity problem at ultra-high field. However, researchers debate whether it is worth installing parallel transmit system for RF shimming applications, and if so, then how much more efficient is the parallel transmit system compared to standard CP systems? To answer these questions, various methods were developed in this work using RF shimming at pTx, and compared with standard CP systems configuration.

INTRODUCTION

In this PhD dissertation, the following two techniques were focused on:

➤ **Employing higher number of Tx channels**

In this method, multi-slice B_1^+ maps were acquired and RF shimming experiments were performed on these B_1^+ maps with different independent transmit (Tx) channel configuration from 1-channel Tx (CP mode) to 2-, 4-, and 8-channel Tx. The resulting benefit in brain imaging fidelity (improvement in B_1^+ homogeneity and reduction in RF-power) was studied.

➤ **Global and slice-selective RF shimming**

In this approach, the RF shimming algorithm was performed in two different ways. First, one set of RF shim values was optimized for the whole excited volume (global RF shimming) and afterwards, the individual sets of RF shim values were optimized for individual slices (slice selective shim). The purpose of using slice selective RF shimming is to segment the volume into several slices, thereby reducing the RF shim region of interest (ROI) from the whole brain to individual slices of the brain.

Another goal of this study was to evaluate the feasibility of trading homogeneity for RF-power or vice versa, using different numbers of Tx channels and shimming methods, and to compare it with the CP mode used in current standard MR systems.

2

Background

In this chapter, a brief background of the relevant concepts is presented in order to understand the context of this dissertation. The general principles of MRI are described, followed by the theory behind RF transmission in single and multi-channel systems. The theories behind effects of B_1^+ inhomogeneity on contrast and reduction of B_1^+ inhomogeneity have also been discussed.

2.1. Magnetic Resonance Imaging

Signal Origin

MRI takes advantage of the phenomenon of nuclear spin angular momentum, which is present in nuclei having odd number of protons or neutrons. These nuclear spins have a magnetic dipole moment, which can be controlled and manipulated using magnetic fields.

BACKGROUND

In the highly aqueous human body, the hydrogen nuclei in water molecules possess this spin behavior, and are responsible for the signal in conventional MR imaging. As the water content varies in different parts of the body, so does the hydrogen concentration and the resulting magnetization. Therefore, signals obtained from different parts of the body are unique and characteristic. For example, the white and gray matters of the brain provide very different signals, resulting in a contrast image which is very useful for clinical MR imaging.

Signal generation and detection

There are two phases in the MRI process. The initial excitation phase involves exciting magnetic moments from their minimum energy state to higher energy states, resulting in the generation of a signal. In the subsequent acquisition phase, the signal is detected via induction, encoded, and collected as the spins relax back to the minimum energy state. Magnetic fields are used in MR imaging to align, excite and control the nuclear spins. There are three types of fields employed for this purpose, the main magnetic field B_0 , RF field or B_1 field and gradient field.

A constant main field, B_0 , is continually applied along the positive z-direction. This strong and static magnetic field produces two main effects. Firstly, the randomly oriented magnetic moments align with the applied magnetic field. Secondly, the excited magnetic moments start to precess at the Larmor frequency. This frequency, ω , has a linear relationship to the strength of the applied field,

BACKGROUND

Equation 2.1:

$$\omega = \gamma B_0$$

where γ is the gyro magnetic ratio. For any given nucleus, the gyro magnetic ratio has a constant value. For ^1H , $\frac{\gamma}{2\pi} = 42.58 \text{ MHz/Tesla}$; so the Larmor frequency is 127.74 MHz for the magnetic field strength of 3T. The B_0 field polarizes the net magnetization in the z-direction with the strength of M_0 [52].

The spins are excited at the Larmor frequency using the RF field or B_1^+ field. Using RF transmission coil(s), the RF pulse is applied in the x-y (transverse) plane. Therefore, the RF excitation causes a rotation of M by a certain angle. A torque is induced on the magnetization by the rotating magnetic field B_1 , and this causes M to rotate away from its equilibrium position along z, while proceeding about the z axis. Eventually, M returns to its position of equilibrium along the z axis due to regrowth of the longitudinal component, M_z . The return of the magnetization vector along the z direction is characterized by the time constant T_1 . The regrowth of M_z is accompanied by the simultaneous decaying of the transverse component, M_{xy} . The time constant T_2 characterizes the decay of the vector component in the transverse plane (x-y plane).

If the spins experience only B_0 field and are excited by B_1 fields, then the generated signals would be indistinguishable after excitation at different locations. In MRI, applying a linear gradient magnetic field in addition to B_1 and B_0 fields is required to achieve spatial localization. Time varying gradients are generally used. Therefore, the spin frequencies would be a function of spatial location.

BACKGROUND

In the below equation, let $\mathbf{G}(t)$ be a gradient field oriented in 3D, which consists of three vector components: $G_x\mathbf{i}$, $G_y\mathbf{j}$ and $G_z\mathbf{k}$. When the three gradient fields are all turned on, the overall magnetic field can be calculated as

Equation 2.2:

$$B(r, t) = (B_0 + G(t) \cdot r)k$$

Thus, the transverse component derived from the Bloch equation becomes

Equation 2.3:

$$M(r, t) = M_0(r)e^{-t/T_2(r)}e^{-i\omega_0 t}e^{-i\int_0^t \Delta\omega(r, \tau) d\tau}$$

where $\Delta\omega(r, t) = \gamma\Delta B(r, t)$.

During the acquisition phase, it is essential to be able to differentiate between signals from various spatial locations in order to create an image. In the presence of gradient fields, the magnetic moments at different locations spin at different frequencies. Therefore, the resultant frequencies detected during the acquisition phase vary.

2.2. RF excitation

In the presence of the B_0 field, an external force is created by the oscillating magnetic field, $\mathbf{B}_1(t)$, which rotates with the Larmor frequency. According to the quantum mechanical model (Planck's law), electromagnetic radiation of frequency ω_{rf} has energy equal to:

BACKGROUND

Equation 2.4:

$$E_{rf} = \hbar\omega_{rf}$$

In order to induce spin transition from one energy state to another, energy of the radiation must equal the energy difference, ΔE , between the adjacent energy states.

This can be represented by the below equation:

Equation 2.5:

$$\hbar\omega_{rf} = \Delta E = \gamma\hbar B_0$$

or

Equation 2.6:

$$\omega_{rf} = \omega_0$$

This equation (2.6) represents the resonance condition. In MR scanning, the RF pulse is turned on in the presence of B_0 magnetic field, which causes identical spin excitation through the entire volume. This is known as a global or non-selective excitation. In most cases, a slice selective gradient is used with the RF, which causes spin excitation in a specific region of the volume only, typically in a plane. This is called selective excitation.

2.2.1. Basic excitation principles

The most basic form of excitation is a whole volume excitation, with a RF field B_1 tuned to the Larmor frequency in the presence of only the B_0 field. There is no restricted region of excitation here.

BACKGROUND

An amplitude-modulated RF pulse, $\mathbf{B}_1(t)$, which is applied in the transverse direction, can be considered the general form of excitation. $\mathbf{B}_1(t)$ is typically in a linear polarized magnetic field and can be represented by the below equation [53]:

Equation 2.7:

$$\mathbf{B}_1(t) = 2B_1(t) \cos \omega_{rf} t \mathbf{i}$$

where, $B_1(t)$ is called the amplitude modulation function or the pulse envelop function, and ω_{rf} indicates the excitation carrier frequency. This linearly polarized field gives rise to two circularly polarized fields, rotating in the clockwise and counter-clockwise directions. The $\mathbf{B}_1(t)$ field can be mathematically represented by the below equation:

Equation 2.8:

$$\mathbf{B}_1(t) = B_1(t)[\cos \omega_{rf} t \mathbf{i} - \sin \omega_{rf} t \mathbf{j}] + B_1(t)[\cos \omega_{rf} t \mathbf{i} + \sin \omega_{rf} t \mathbf{j}]$$

where the clockwise rotating field is the first bracketed term and the counter-clockwise rotating field is represented by the second bracketed term. The two fields are named $B_1^+(t)$ and $B_1^-(t)$, for their counter-clockwise and clockwise rotating directions, respectively [54]. As the counter-clockwise component has no significant effect on the spins [52,53], the $\mathbf{B}_1(t)$ field effectively becomes:

Equation 2.9:

$$\mathbf{B}_1(t) = B_1(t)[\cos \omega_{rf} t \mathbf{i} - \sin \omega_{rf} t \mathbf{j}]$$

The x-component of the field is given by:

Equation 2.10:

$$B_{1,x}(t) = B_1(t) \cos(\omega_{rf} t)$$

And the y-component can be represented as:

BACKGROUND

Equation 2.11:

$$B_{1,y}(t) = -B_1(t) \sin(\omega_{rf}t)$$

Thus, $\mathbf{B}_1(t)$ can be represented in complex notation as:

Equation 2.12:

$$\mathbf{B}_1(t) = B_1(t)e^{-i\omega_{rf}t}$$

In summary, an oscillating $\mathbf{B}_1(t)$ field is generated by the RF pulse, perpendicular to the \mathbf{B}_0 field. Assuming zero initial phase, the RF pulse is characterized by: $B_1(t)$, the envelope function and ω_{rf} , the carrier or excitation frequency. The parameter, ω_{rf} , is generally constant and depends on the resonance condition. The envelope function is the most important part of the RF pulse as it defines the shape and duration of the pulse, thus characterizing its excitation property.

Rotating frame

The excitation effect of an RF pulse can be simply described using the rotating frame of reference where the transverse x-y plane rotates in clockwise direction about the z axis with an angular frequency, ω . Assuming x' , y' , and z' represent a rotating frame and i' , j' , and k' are the corresponding unit vectors along the three axes, then the rotating frame can be represented in laboratory frame by the following equations:

Equation 2.13:

$$\mathbf{i}' = \cos(\omega t) \mathbf{i} - \sin(\omega t) \mathbf{j}$$

$$\mathbf{j}' = \sin(\omega t) \mathbf{i} + \cos(\omega t) \mathbf{j}$$

$$\mathbf{k}' = \mathbf{k}$$

The magnetization in the laboratory frame, \mathbf{M} , can be denoted by:

BACKGROUND

Equation 2.14:

$$\mathbf{M} = M_x \mathbf{i} + M_y \mathbf{j} + M_z \mathbf{k}$$

The magnetization in the rotating frame, \mathbf{M}_{rot} , can be given by:

Equation 2.15:

$$M_{rot} = M_x \mathbf{i}' + M_y \mathbf{j}' + M_z \mathbf{k}'$$

Assuming $\mathbf{M} = \mathbf{M}_{rot}$, the result is

Equation 2.16:

$$\begin{bmatrix} M_{x'} \\ M_{y'} \\ M_{z'} \end{bmatrix} = \begin{bmatrix} \cos(\omega t) & -\sin(\omega t) & 0 \\ \sin(\omega t) & \cos(\omega t) & 0 \\ 0 & 0 & 1 \end{bmatrix} \begin{bmatrix} M_x \\ M_y \\ M_z \end{bmatrix}$$

Similarly, for \mathbf{B}_1 and $\mathbf{B}_{1,rot}$

Equation 2.17:

$$\mathbf{B}_1 = B_{1,x} \mathbf{i} + B_{1,y} \mathbf{j}$$

and

Equation 2.18:

$$\mathbf{B}_{1,rot} = B_{1,x} \mathbf{i}' + B_{1,y} \mathbf{j}'$$

Then

Equation 2.19:

$$\begin{bmatrix} B_{1,x'} \\ B_{1,y'} \end{bmatrix} = \begin{bmatrix} \cos(\omega t) & -\sin(\omega t) \\ \sin(\omega t) & \cos(\omega t) \end{bmatrix} \begin{bmatrix} B_{1,x} \\ B_{1,y} \end{bmatrix}$$

The magnetization vector and \mathbf{B}_1 can be interconverted between the laboratory and rotating frames using equations 2.16 and 2.19. This transformation can also be represented in complex notation as:

BACKGROUND

Equation 2.20:

$$M_{x'iy'} = M_{xy}e^{i\omega t}$$

where $M_{xy} = M_x + iM_y$ and $M_{x'iy'} = M_{x'} + iM_{y'}$ and

Equation 2.21:

$$B_{1,rot} = B_1(t)e^{i\omega t}$$

where $B_1 = B_{1,x} + iB_{1,y}$ and $B_{1,rot} = B_{1,x'} + iB_{1,y'}$

The relaxation terms can be ignored to simplify the Bloch equation in the rotating frame as:

Equation 2.22:

$$\frac{\partial \mathbf{M}_{rot}}{\partial t} = \gamma \mathbf{M}_{rot} \times \mathbf{B}_{eff}$$

where

Equation 2.23:

$$\mathbf{B}_{eff} = \mathbf{B}_{rot} + \frac{\omega}{\gamma}$$

When $\mathbf{B}_1(t)$ is tuned to the Larmor frequency, the excitation is called on resonance excitation. In this state, the RF pulse in the presence of B_0 field, excites all the spins in the entire volume. On the other hand, in the selective excitation approach, excitation of only the desired region is achieved by turning on the RF pulse with the modulation function $\mathbf{B}_1(t)$, in the presence of gradient magnetic field G_z [55]. As a result, only the spins lying in the z direction having resonance frequencies matching the temporal frequencies of $\mathbf{B}_1(t)$ will be excited. The spins with resonance frequencies that are outside the excitation bandwidth will not be excited.

B₁⁺ field inhomogeneity

The most challenging aspect at high field is B₁⁺ inhomogeneity. The high static B₀ fields can cause spatial variation in B₁⁺ during excitation, and this phenomenon is known as B₁⁺ inhomogeneity. During MR sequences, this B₁⁺ inhomogeneity will result in a non-uniform distribution of the desired flip angles across spatial locations, thus causing the image intensity to vary as a function of space.

The RF frequencies required for resonance oscillation in 3T and 7T MRI scanners are roughly 128 MHz and 300 MHz, respectively. During propagation of the B₁⁺ field through any medium, the wavelengths are shorter and their amplitudes are attenuated, as compared to free space propagation. This can be represented by the complex wave number and the plane-wave equations shown below. The complex wave number [56] is given by Maxwell's equation as below:

Equation 2.24:

$$\kappa = \kappa_+ + i\kappa_- \quad \kappa_{\pm} = \omega \sqrt{\frac{\epsilon\mu}{2} \left[\sqrt{1 + \left(\frac{\sigma}{\epsilon\omega}\right)^2} \pm 1 \right]^{\frac{1}{2}}}$$

From the above equation 2.24, plane-wave solutions can be derived as:

Equation 2.25:

$$E(x, t) = E_0 e^{i(kx - \omega t)}, \quad B = B_0 e^{i(kx - \omega t)}$$

As seen from these equations, substituting the complex wave number k in the plane-wave solutions, results in the imaginary part of k becoming a negative real number and exponential decaying of the wave-amplitude as the wave travels through a medium. The

BACKGROUND

real part of k , on the other hand, becomes an imaginary number which determines the wavelength, propagation speed, and refractive index. This wavelength is represented by the below equation:

Equation 2.26:

$$\lambda = \frac{2\pi}{\kappa_+}$$

For a “poor” conductor

$$\sigma \ll \omega\epsilon$$

Equation 2.27:

$$\kappa_+ \cong \omega\sqrt{\epsilon\mu}, \quad \kappa_- \cong \frac{\sigma}{2} \sqrt{\frac{\mu}{\epsilon}}$$

where σ = conductivity

ω = RF frequency

ϵ = Permittivity

μ = Permeability

The above equation indicates that wave penetration through this medium does not depend on the frequency, and the standing waves created inside the medium will affect B_1 inhomogeneity.

For a “good” conductor $\sigma \gg \omega\epsilon$

Equation 2.28:

$$\kappa_+ \cong \kappa_- \cong \sqrt{\frac{\omega\sigma\mu}{2}}$$

For a medium having moderate conductivity, the complex wave number can be calculated from the original equation (2.24). In distilled water having zero conductivity

BACKGROUND

and a high dielectric constant, the B_1 field's wavelength is reduced to 27 cm at 300 MHz [57] which is comparable to the size of a human head. Conducting the experiment in a distilled-water phantom of this size would produce a standing wave inside the phantom, and would result in an inhomogeneous RF distribution. However, in human brain tissue, which has moderate conductivity [58], the strong decay of the RF due to sample conductivity (the κ - term) will not allow a sustained standing wave. The amplitude distribution of the magnetic fields in the head depends on the decaying traveling waves in a given coil configuration as well as dielectrically induced standing waves. This results in variations in the signal intensity, with higher intensity in the middle of the image and decreased intensity towards the edges. The inhomogeneity effect is more severe during ultra-high field imaging [29,59]. Optimization of the homogeneous RF excitation is the solution for lowering this B_1^+ inhomogeneity, as will be discussed in the following subsections.

2.2.2. Excitation methods in MR

During the excitation phase, the number of transmit coil elements plays an important role in localizing specific regions of interest. In this subsection, single-channel and multi-channel excitation concepts are described. Controlling the RF field with a multi-channel design is also explained.

2.2.2.1. Excitation in standard single channel transmit MRI

In standard single channel MRI or CP system, a single RF generator generates the B_1^+ field which excites a spin system; this in turn generates a signal, which can be measured by the receive coils. The amplitude and phase of the RF pulse can be only controlled by a single RF amplifier. When higher number of Tx coil elements are used, the transmitted field is the vector sum of all the fields. The flexibility of a system with multiple Tx coil elements is thus exemplified by the fact that it can globally alter the Tx field.

During the excitation phase in single channel MRI the time-dependent behavior of magnetic moments \vec{M} can be quantitatively described by the Bloch equation [60]. This equation represents the magnetization state after excitation with RF pulse B_1 , for a given initial magnetization state M_0 . The Bloch equation can be used in the context of MRI as,

Equation 2.29:

$$\frac{\partial M_{rot}}{\partial t} = \gamma M_{rot} \times B_{eff} - \frac{M_x i + M_y j}{T_2} - \frac{(M_z - M_0) k}{T_1}$$

where γ is the gyromagnetic ratio, T_1 and T_2 are the relaxation time constants in the longitudinal and transverse directions respectively, and M_0 is the initial magnetization state (which is aligned to the positive z-axis in the presence of B_0 field). However, equation 2.29 is non-linear. Thus, it is difficult to use this equation to design RF excitation pulses (B_1) [10]. However, for short excitation pulses, the relaxation effects (T_1 & T_2) can be ignored. Also, for small tip angles, the ‘small tip angle approximation’

BACKGROUND

[61] can be used to provide a linear equation which represents the transverse (x-y) magnetization (m_{xy}) due to the RF pulse envelope, $\mathbf{B}_1(t)$ as a function of spatial position (r) [10].

Equation 2.30:

$$m_{xy}(\vec{r}) = i\gamma m_0 \int_0^T B_1(t) e^{i\vec{r}\vec{k}(t)} dt$$

Where

Equation 2.31:

$$\vec{k}(t) = -\gamma \int_t^T \vec{G}(s) ds$$

The equation 2.30 shows the gradient field (\vec{G}) and RF excitation pulse that can be used to control the m_{xy} at various location of the image, and a Fourier relation between the transverse magnetization (m_{xy}) and the RF pulse envelop (B_1). It gives detailed description of RF excitation where the gradient field ($\vec{G}(t)$) is used to traverse a path in Fourier space (“excitation k -space”), while $\mathbf{B}_1(t)$ describes the weighting (deposition of RF energy) of the excitation k -space along this path [10].

In single channel transmission, the homogeneous birdcage-type body-coil is commonly used and has served the MRI community well. However, it does not possess spatial degrees of freedom, and subsequently not works best for uniform excitations at ultra high field MR.

2.2.2.2. Excitation using parallel transmit system

The parallel transmission system is an important form of RF transmission, where spatial distribution of the transmit coils is in a parallel fashion. Each individual transmit element of coil has an individual RF generator. Dividing the transmit field into multiple regions that are individually controlled by separate transmit channels creates spatial degrees of freedom. Parallel excitation arrays, along with the ability to utilize the spatial information in an array during RF transmission, offer the possibility to move beyond the uniform slice-select excitation. Parallel excitation also allows for spatially tailored RF pulses, which are excitation pulses with a carefully controlled spatially varying flip angle (FA). These tailored RF pulses can mitigate artifacts or isolate specific anatomy.

Mathematically, the RF field produced by a single channel can be formulated as a separable function of time and space,

Equation 2.33:

$$B_1(\mathbf{r}, t) = S(\mathbf{r})B_1^+(t)$$

Here $S(\mathbf{r})$ is the complex transmit sensitivity of the single channel. This equation can be extended for excitation in parallel fashion by,

Equation 2.34:

$$B_1(\mathbf{r}, t) = \sum_{n=1}^N S_n(\mathbf{r})B_{1,n}^+(t)$$

The B_1^+ sensitivity profile refers to the spatial variation produced in the RF field when a current is applied to the coil. This sensitivity profile depends on the shape and position of the coil. In the single-channel transmission case, the RF coil is designed in such a

BACKGROUND

way that its sensitivity profile remains uniform across the space. Generally, a “birdcage” coil designed to produce a uniform field is used for this purpose. (Note: the uniform birdcage mode’s RF field is not homogenous at high B_0 field, hence leads to B_1^+ inhomogeneity problem).

RF coil: An important consideration in MR imaging is the RF coil(s). The nuclear spins absorb RF energy from a pulse generated by the RF transmit coil [62]. When the pulse is switched off, the energy from the spins is detected by a receive coil. While the same coil can be used for both purposes, transmission and reception, separate coils are often used in order to optimize the image quality [10]. The RF coils for single channel and parallel transmit system are different. In the RF coil of single channel system, all transmit elements are connected to single RF generator. In the RF coil for parallel transmit system, each coil transmit element is connected to an individual RF generator.

2.3. RF shimming

Higher B_0 field brings higher B_1^+ inhomogeneity in to the image this is explained in previous subsection. This B_1^+ inhomogeneity can be carefully control by parallel transmit hardware [63]. Many methods have been proposed for parallel RF excitation to reduce the B_1^+ inhomogeneity from the image. In the method presented by Katscher et al. [34], the system of linear equations are solved in the excitation Fourier space, k -space. On the other hand, the scheme developed by Zhu [36] was formulated in the spatial domain with the assumption of an echo-planar k -space trajectory. Another

BACKGROUND

method proposed by Griswold et al. [64] draws on the “GRAPPA” technique [65] used in accelerating data acquisition with receive arrays, and is solved in the k-space domain. Finally, Grissom *et al.* [66] formulated the design as a direct discretization of the parallel small tip angle equation in space and time.

The RF shimming at parallel excitation approximation can be obtained by substituting Equation 2.34 into Equation 2.30,

Equation 2.35:

$$m_{xy}(\vec{r}) = i\gamma m_0 \sum_{c=1}^C S_c(\vec{r}) \int_0^T b_{1,c}(t) e^{i\vec{r}\vec{k}(t)} dt$$

where, the resulting overall magnetization is the sum of the individual magnetizations in each of the coils. The additional term $S_c(\vec{r})$ in this equation reflects the coils' B_1^+ sensitivity profiles. In the case of single coil systems, the sensitivity profile was assumed to be uniform in space, and hence it was not included in Equation 2.30.

2.3.1. Static RF shimming

In Equation 2.24, by discretization of space and time, a matrix version can be derived, $m=Ab$, where m is the target profile in space, A is the matrix which includes the B_1^+ coil profiles modulated by the Fourier kernel due to the k-space traversal, and b is the complex weighting factor, which contains amplitude and phase of the RF pulse. Using this equation, the static RF shim can be optimized after applying the conventional Least Squares (LS) algorithm:

Equation 2.36:

$$\delta = \arg_b \min\{\|Ab - m\|_w^2 + R(b)\}$$

Where, w is the weighting factor for the Region of Interest, and $R(b)$ is the Tikhonov regularization term ($R(b) = \lambda b'b$) used to control integrated and peak RF power. This equation optimizes term b that is complex value which is amplitude and phase of the RF pulse, and it is used for homogenizing the magnetic field. This method of homogenization is called static RF shimming.

2.3.2. Transmit-SENSE

The imaging SENSE method [67] makes use of the unique receive-sensitivity profiles of the coil-elements and reconstructs the un-aliased image from an acquisition with reduced k-space [68]. Similarly, Transmit sensitivity encoding (SENSE) [34,36,69] makes it possible to reach the desired target excitation with a reduced k-space sampling during RF transmission. As a result, it is possible to design shorter excitations without compromising the desired excitation fidelity [34,36,66]. This simultaneously allows the inclusion of multidimensional RF-pulses in fast sequences having short repetition times, while lowering the effects of relaxation and off-resonance during the RF pulse.

Multidimensional RF pulse design is based on the principles proposed by [61]. Multidimensional RF pulse design was initially formulated in the frequency domain [34], and later used in the spatial domain, with EP trajectories only [36]. The spatial domain method proposed by Grissom [66], is the most widely used method currently. This

BACKGROUND

approach permits arbitrary shapes for k-space trajectories and takes the measured off-resonance effects into account.

Trajectories through k-space

The “fast-kz” trajectory method [70] is the most extensively studied among the various methods [44,71–73]. This trajectory is designed to allow relatively short pulse durations in slice-selective uniform excitations. This method resides in the combination of a dense k-space sampling along the slice direction interleaved with a few short gradient blips orthogonal to this direction [74]. When the fast-kz trajectory is viewed through k-space, it resembles a set of spokes (Figure 1), giving rise to the nickname “spokes”. As a fixed bandwidth is necessary to provide the desired slice profile, the RF sub-pulses associated with each spoke have a fixed duration. Therefore, optimally selected spoke locations are required in order to minimize the pulse duration [71–73].

Slice-selection is performed with the spoke trajectory by depositing sinc-like RF pulses along each transversal “kz-spoke”. These sinc-like RF pulses have complex amplitudes which are designed to give the desired in-plane excitation modulation for B_1^+ mitigation. According to the Fourier theory, a spoke can provide in-plane modulation at an in-plane location \bar{k}_s having a RF complex amplitude of $A_s e^{j\phi_s}$, which can be represented by $[A_s e^{j\phi_s}] e^{j2\pi\bar{k}_s \cdot \bar{r}}$. Therefore, the total in-plane modulation for an excitation trajectory with N_s spokes can be given by the below equation

BACKGROUND

Equation 2.37:

$$E(\vec{r}) = \sum_{S=1}^{N_s} [A_s e^{j\phi_s}] e^{j2\pi\vec{k}_s \cdot \vec{r}}$$

Thus, by using a sufficiently large number of spokes with appropriately tailored complex amplitude, it is possible to create the desired excitation modulation, which is an inverse pattern of the inhomogeneity. In parallel transmit systems, these spokes pulses can be design for each individual transmit channel. This is illustrated in Figure 1 using an example with parallel transmission, where the eight elements of the stripline array coil are each driven separately. In this case, the parallel excitation uses 8 spokes to provide 8 bases per RF channel, thus providing a total of 64 bases for the entire 8 RF channels setup. Using these bases can provide a similar level of mitigation with much shorter excitation duration, as compared to the single channel case.

BACKGROUND

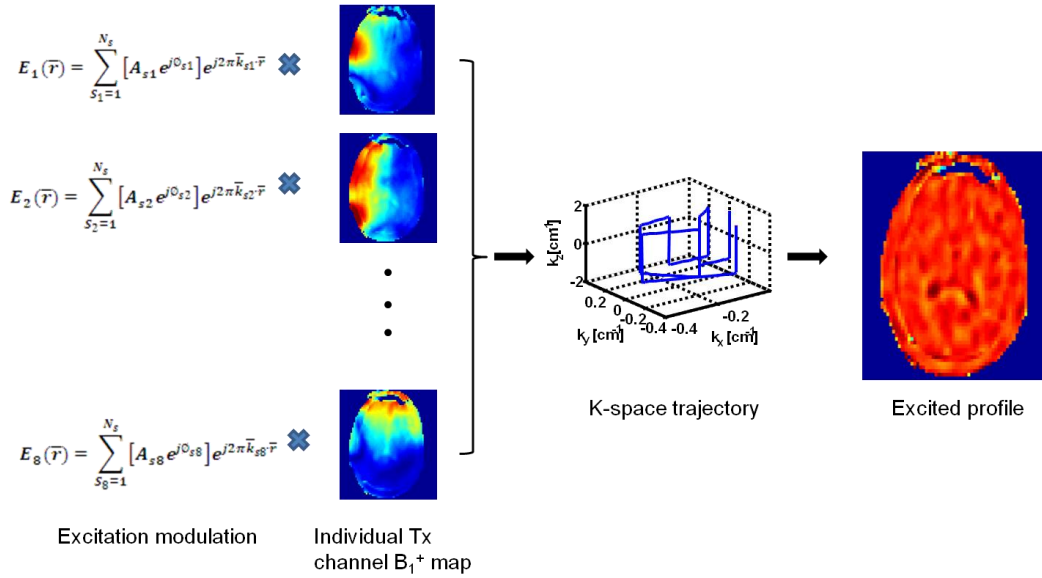


Figure 1: K-space trajectory considered for pTx applications, addressing a slice selective spokes.

In this dissertation, the use of parallel transmission arrays with RF shimming for volume imaging is proposed as a suitable method to reduce FA variation and correct for this inhomogeneous contrast. The effects of RF shimming in parallel transmission were thoroughly investigated in this study. This proposed approach was found to bring about a significant reduction in peak RF-power and improvement in the B_1^+ homogeneity for excited volumes, as compared to standard single channel MR system.

While the focus of this work is on transmit field inhomogeneity, it is also important to mention that the RF receive profile (B_1^-) can exhibit spatial inhomogeneity at high B_0 field as well. However, the B_1^- inhomogeneity causes variation only in image intensity

BACKGROUND

and SNR, while the B_1^+ homogeneity causes variations in image contrasts. While the loss in SNR can often be problematic, this variation is not as critical an issue as image contrast problems. The SNR variation can be removed by a point by point division of the image by the B_1^- profile, but it is possible that this correction method could produce spatially varying SNR [10].

Materials and Methods

In this section, the various methods and experimental details used in this dissertation are described in detail. The overall experimental setup such as hardware requirements and general methods are described initially. The fast B_1^+ mapping method is then detailed with individual Tx channel B_1^+ maps. The RF shimming method used in this work is then explained. The application of the above methods to imaging the brain volume is then described. Various techniques used in combination such as slice selective RF shimming, global RF shimming and higher Tx channels, are also described in detail. This section also explains how various combinations of Tx channels were configured.

3.1. Experimental Setup

All measurements were performed on a 7T MR scanner (Siemens Erlangen, Germany) with SC72AB gradient coil (Siemens Erlangen, Germany). This system was built around 60-cm-diameter-bore superconducting magnet connected to a Syngo console. The

MATERIALS AND METHODS

whole-body gradient coil had diameter of 60 cm inside the magnet which provides a maximum gradient strength of $70 \text{ mT m}^{-1} \text{ s}^{-1}$ at MRI system.

Parallel transmit system: The 7T MR system used in this study has a pTx extension with eight independent RF-pathways (Siemens). The 7T system architecture is briefly described here for better understanding of the results obtained in later sections (Figure 2). In the system, there are eight independent modulators, each attached to its own power amplifier, providing up to 1-kW peak power apiece. Using a directional coupler, the power output of each amplifier is monitored in real-time, allowing the peak, 10-s, and 6-min averaged power to be constrained. (TALES for channels 1 through 7 are located in the service room, whereas the monitor for channel 8 is located inside the scanner). As a safety feature, if any of the pre-specified power limits is exceeded, the acquisition is terminated. Safety tests were performed to evaluate the stability of the RF-waveform under different conditions before performing in-vivo experiments, and also the appropriate time-averaged power limits were derived such that compliance with the SAR guidelines was ensured.

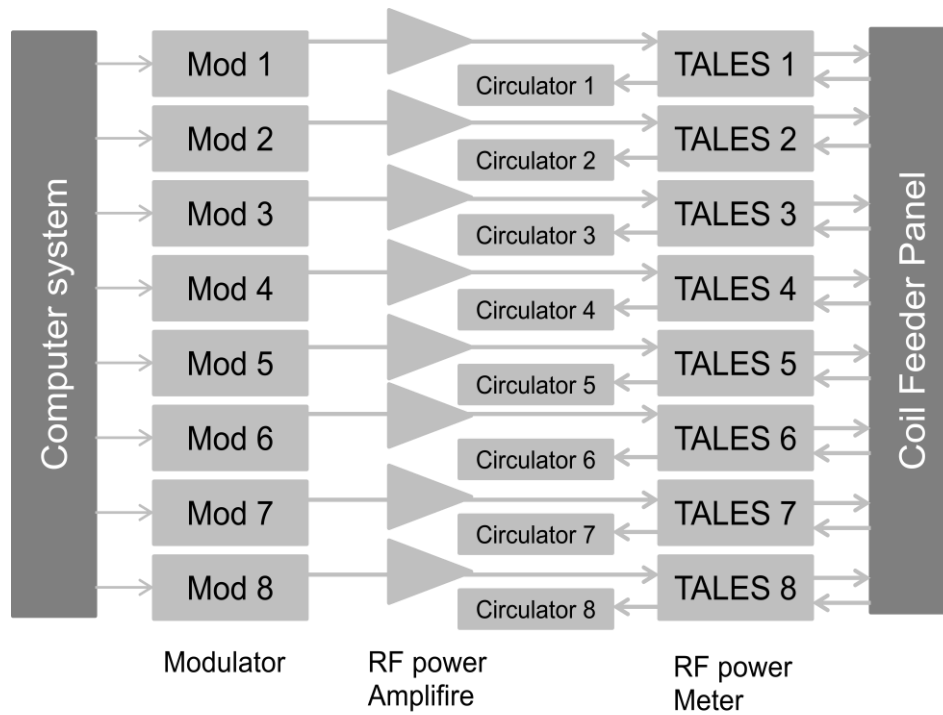


Figure 2: A schematic representation of the RF pathway is shown for the 8-channel pTx-extension. The individual transmit-channels have their own separate modulator (this includes the mixing to the 297MHz carrier frequency) and amplifier, and the forward power from each individual amplifier is monitored (peak, 10-sec-, and 6-min-averaged power). Acquisition is terminated if any of the associated pre-defined limits are exceeded. Channels 1 through 7 have power monitors situated in the service room, while the monitor for channel 8 is situated inside the scanner.

RF coil array

Parallel transmit hardware requires special coils that are capable of driving individual RF pulses through individual Tx channels of the coil. A standard 8-channel Tx/Rx Rapid and an 8/32-channel Tx/Rx QED body coil were used for the parallel transmission experiments in this study.

RAPID 8 Tx/Rx head coil: For brain imaging experiments, an oval cylinder shaped eight-channel loop coil array (Rapid Biomedical, Rimpar, Germany) was used for transmission and reception. The dimensions of the coil array were; 24 cm length, 28 cm width and 31.5 cm height. The signal was received from the same eight coils in an array reception mode. This head coil consists of 8-shielded elements without capacitive or inductive decoupling.

QED 8 TX/32 RX coil: For abdominal MRI at 7T, an 8Tx/32 Rx RF coil (QED, Mayfield Village, OH) was used, consisting of an anterior and a posterior part. Each part comprises of 4 parallel strip line Tx elements oriented in head-foot-direction, and 16 Rx coils in loop design, arranged in a 4x4 array. The coil was modeled in SEMCAD X (Schmid & Partner Engineering AG, Zürich, Switzerland) with in-plane resolution of ≤ 0.5 mm and ≤ 2 mm in z-direction, together with the whole body virtual human Duke (Virtual Family [75], IT'IS Foundation) with ≤ 3 mm isotropic resolution (Figure 3 Top). The local SAR for each element was simulated and averaged over 10 cm³ (Figure 3 Bottom). The coil was connected to a 7T MR system equipped with an 8-channel pTx

MATERIALS AND METHODS

console (Siemens Healthcare, Erlangen, Germany). For volunteer imaging, the coil halves were placed at the level of the kidneys.

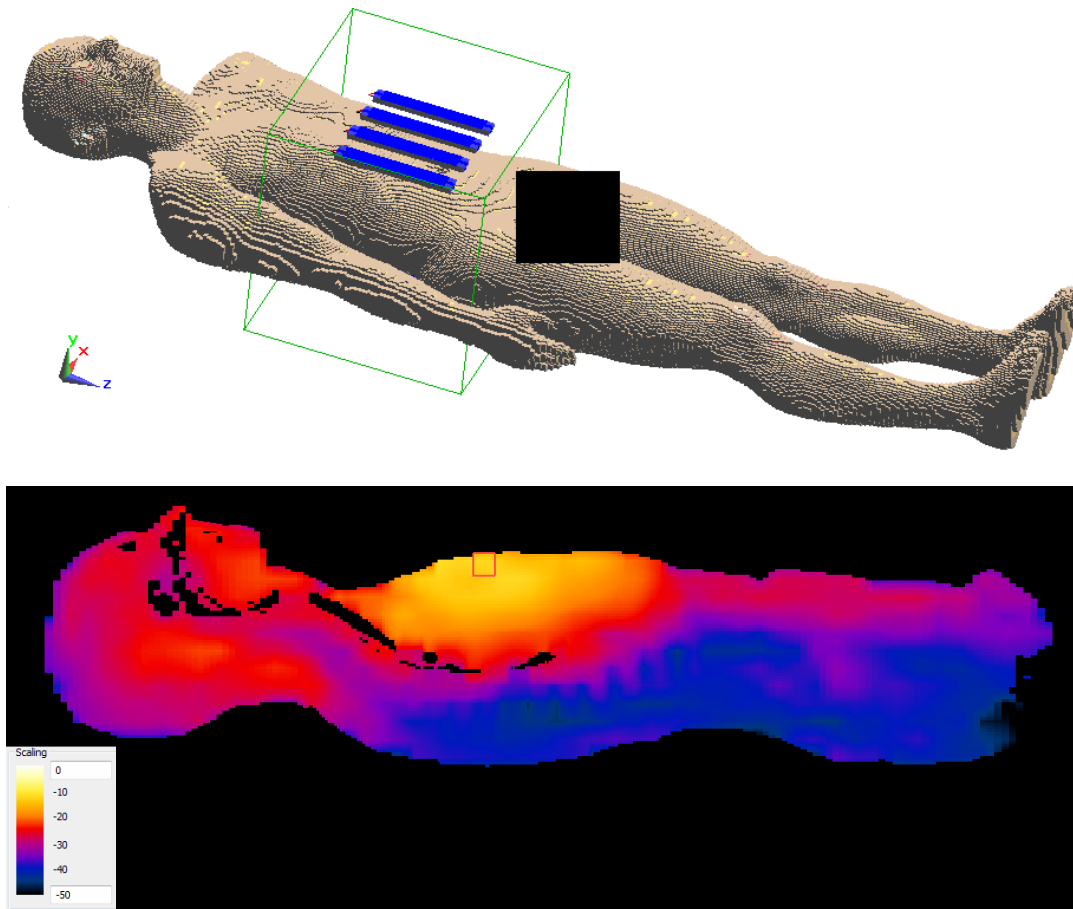


Figure 3: Voxel model of virtual human and placement of anterior transmit elements (Top). Local SAR distribution of a single Tx element, 10 cm³ average (Bottom) (Figure courtesy of Schmid & Partner Engineering AG, Zürich, Switzerland).

SAR monitoring: For the experiments conducted in this study, two 8 channel coils were obtained from the same vendor (RAPID) with same geometry, one for single channel (CP system) and another for parallel transmit system. The SAR simulations for the CP system coil predict a maximum local SAR of 10 W/kg for a global SAR of 1.87 W/kg. Assuming a head weight of approximately 5.25 kg, the maximum value of total forward power of 9.87 W was obtained to comply with IEC guidelines.

In the case of the 8 channel Tx coil, SAR can increase locally up to 8 times if the electric fields of all 8 elements constructively superimpose, since SAR is proportional to the square of the electric field. Therefore, the maximum forward power was divided by a safety factor of 8 to ensure safe operation in the 8 channels [76]. In the Tx mode, assuming a worst case scenario in all the positions in the head, a maximum of 1.23 W total forward power is permitted. Based on this, conservative RF power limits of 0.15 W for 6 minutes average RF power per channel were used in this study. A 10 seconds average RF power limit can be up to 3 times higher than the 6 minutes average power value according to IEC. So, 0.30 W (twice higher than 6 minutes value) for 10 seconds average RF power per channel was used here. If the power for any channel exceeded the limits, the system would immediately shut down the RF power amplifier and stop the sequence, thereby insuring the volunteer's safety. Each of the subsequent sections provides details concerning the MR components most relevant to the work presented in the succeeding chapters.

Computational Resources: The console used to operate the pTx-enabled system consists of 2 computer systems referred to as master and slave. The master controls a single transmit-channel (channel 8), and provides all the necessary tools to configure and prepare a new acquisition. The slave system allows any protocol prepared on the master system to be dispatched to all 8 transmit-pathways.

Furthermore, the RF shim solutions were calculated in MATLAB 2008b (The Mathworks) on a desktop PC (Windows XP, i5 processor CPU 3.8 GHz, 4GB RAM). They are detailed in the subsequent chapters.

3.2. B_1^+ mapping

B_1^+ profiles for the eight transmit coils were obtained by applying a slice-selective, TFL sequence with a saturation pulse applied to a single transmission channel at a time, and then receiving signals from all receive channels independently [77,78]. The sequence diagram of the flip angle encoding is shown in Figure 4.

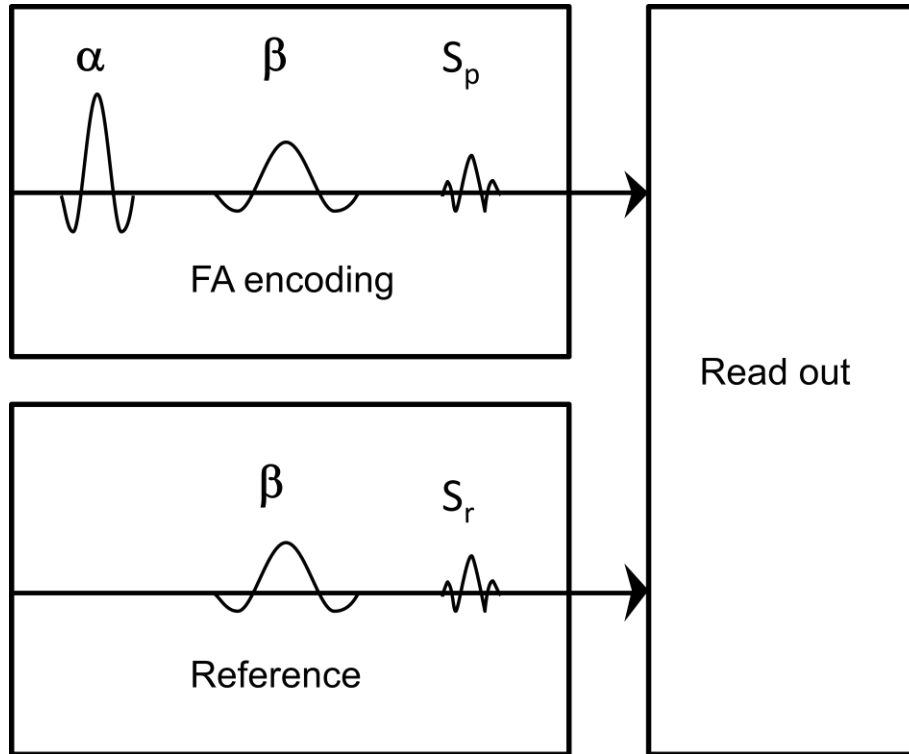


Figure 4: Sequence diagram of modified B_1^+ mapping magnetization prepared TFL sequence.

The RF-pulse α is played out on a single coil element preparing a longitudinal magnetization of

Equation 3.1:

$$M_z(t = 0) * \cos \alpha$$

Transversal magnetization is spoiled with gradients along all 3 spatial dimensions. The longitudinal magnetization is excited by applying a spatially varying flip angle β . It is a composite RF-field generated using all coils of array in the CP phase configuration. The reference image is acquired without magnetization preparation. The signal ratio of the images equals

Equation 3.2:

$$\frac{S_p}{S_r} = (\cos \alpha - 1) * \exp\left(\frac{TD}{T1}\right) + 1 \sim \cos \alpha$$

where S_p = Signal of the image acquired with preparation pulse

S_r = Signal of the reference image

The signal recovery between preparation and excitation was neglected; an α -map (Flip angle map or B_1^+ map) was calculated by taking the inverse cosine of the signal ratio. The relative phases between the RF-field distributions of the different coils were calculated from additional scans using only one coil for excitation. The single coil images were acquired at short TR of 100ms. They are also used for optimizing the phases set to the different coils for the composite β , in order to avoid local low SNR that may be problematic for the signal ratio calculation.

Imaging parameters for the 2D multi-slice TFL sequence were: matrix size $64 \times 64 \times 7$, FOV = 220 mm \times 220 mm, repetition time (TR) = 5000 ms, echo time (TE) = 1.9 ms, 7 slices, distance factor = 100%, slice thickness = 8 mm, TFL read out FA = 8° and acquisition time \sim 50 s. The TFL sequence was further modified to apply optimized RF amplitudes and phases to the appropriate RF pulse and appropriate slice.

Figure 5 below shows the magnitude and phase B_1^+ profiles of eight independent transmit coils, for the 8 Tx/Rx head coil and 8Tx/32Rx body coil. The RF shimming experiments can be performed on it that is presented in following section.

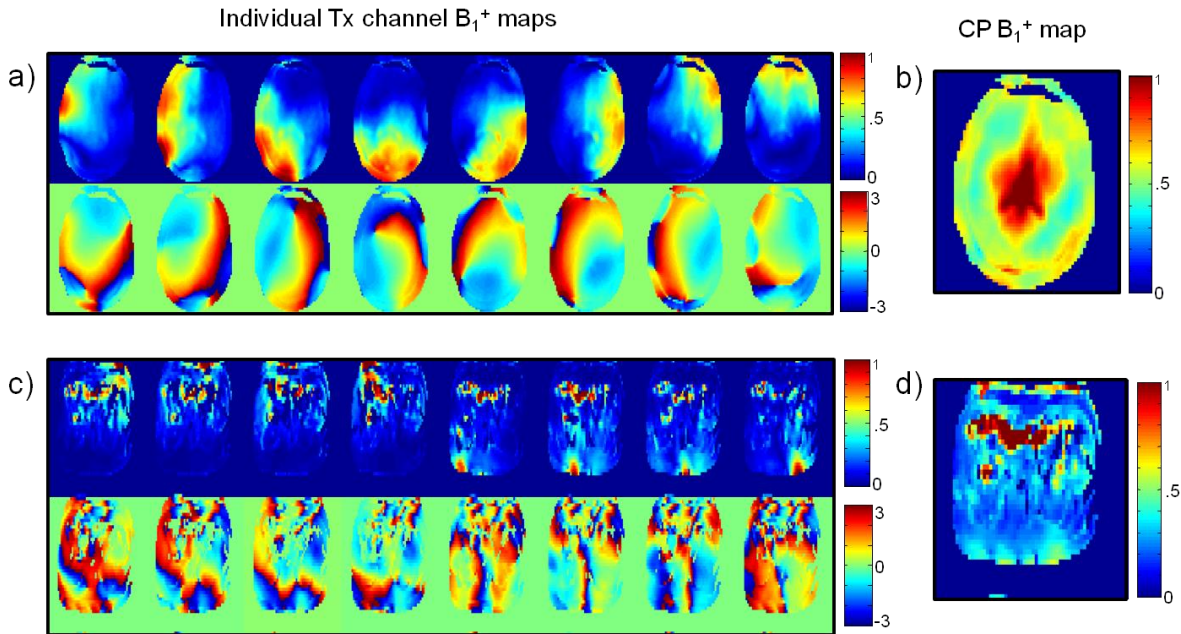


Figure 5: a) and c) shows B₁⁺ profile of individual Tx channel for 8 Tx/Rx head coil and 8Tx/32Rx body coil respectively. The upper panel shows measured magnitude (intensity scale normalized to a maximum value of 1), and the lower panel shows phase (radian) of the individual excitation coil profiles. b) and d) shows CP (combine) B₁⁺ profile of 8 Tx/Rx head coil and 8Tx/32Rx body coil respectively.

3.3. RF shimming

3.3.1. Static RF shimming

In this work, the RF shimming method introduced by Setsempop *et. al.* [79] was employed, which is called magnitude least squares optimization. This method was used in order to improve the magnitude profile and reduce the required RF power, albeit at

MATERIALS AND METHODS

the cost of increased phase variations in the excitation pattern. These low-order spatial phase variations do not pose a significant problem for most excitation applications, such as when magnitude images are recorded. Therefore, the method employed here for RF shim solution calculation uses an adjustable regularization parameter de-emphasizing the excitation phase profile. In order to study the potential benefits in magnitude profile fidelity and RF-power this can accompany the relaxed constraint.

The RF shim values can be obtained from equation (2.36) using a modified magnitude least square error function, δ .

Equation 3.4:

$$\delta = \arg_b \min\{\| |Ab| - m \|^2 + \|\lambda b\|^2\}$$

The A-matrix incorporates vectors containing the B_1^+ profiles of each individual transmit channel; m is the desired excitation field which is an absolute valued vector (for the entire study of RF shimming, m is homogenous), w is weighting, (shows the optimization was performed over selected region of interest); and b is the RF shim solution which contains the complex RF weights and λ denotes a regularization term that may be used to regulate the integrated and peak RF power. In equation (3.4), the dimension of A is $N \times N_c$, where N is the number of voxels and N_c is the number of individual channel. The dimension of m is $N \times 1$ and b is an $N_c \times 1$ dimensional vector containing the complex coil shim solutions for each Tx channel.

3.3.2. pTx spokes RF waveforms

For pTx excitation RF spokes pulses was optimized, where multiple sinc-shaped RF pulses are applied at particular locations in excitation k-space. The spokes trajectory used in this dissertation is shown in Figure 6. This design creates sharp slice selective excitation using sinc-like excitation along k_z axis, and allows modulation of the in-plane (x - y) excitation profile to counter-act the in-plane B_1^+ inhomogeneity. Through amplitude and phase modulation of the different sinc “ k_z spokes” that are placed at various k_x - k_y locations, an excitation pattern is created that is a spatial inverse of the inhomogeneity. Thus, this trajectory choice provides relatively sharp slice profiles (i.e. large extent in k_z) and relatively slowly varying in plane mitigation patterns (i.e. smaller coverage in k_x - k_y) as required for this study.

The MLS optimization given in equation 3.4 was used to find the best amplitude and phase terms for each spokes on each Tx channel (for 2 spokes $2 \cdot 8 = 16$ complex coefficients and for 3 spokes = 24 complex coefficients), such that the mitigated B_1^+ profile is as uniform as possible. The locations of the spokes were determined using a Fourier Transform based iterative automatic placement method [72]. A uniform target profile was used for the spokes pulse calculation. A maximum gradient amplitude of 28 mT/m and a slew rate of 112 mT/m/ms were used for spokes. The regularization parameter λ was used to adjust the RF-power of the spokes pulse, and the duration of spokes pulse was 2 to 3 ms. The magnetization patterns were predicted using a Bloch equation and measured experimentally.

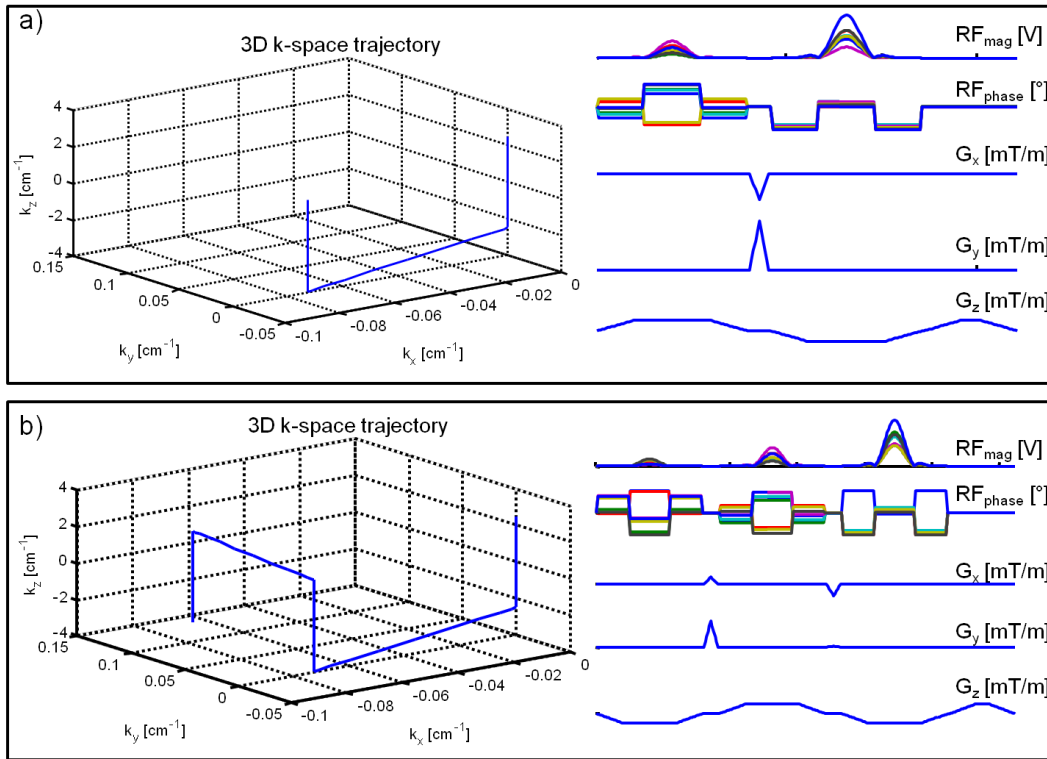


Figure 6: a) and **b)** are the excitation k-space trajectories (shown on the left side of the figure) for a 2-spokes and 3-spokes excitation respectively. The RF and the gradient shapes for the same excitation are presented on the right side of the figure. G_x and G_y gradients are used to get to desired k-space locations, at which times the slice selective RF-sinc pulses (accompanied by G_z gradient for slice selection), are played on each of the 8 transmit channels. The MLS design finds the best amplitude and phase terms for each spoke and each Tx channel (total of 16 or 24 complex coefficients), such that B_1^+ mitigation is as uniform as possible.

RF Shimming Simulation: Simulated B_1^+ maps were generated based on the measured individual transmit coil B_1^+ maps, for static RF shimming and spokes trajectories. Simplified version of equation (2.24) $m = Ab$ was used to simulated RF shimmed B_1^+ profile. In this equation experimented individual Tx channel B_1^+ maps were given as A-matrix, b was optimized from Equation 3.4 and m is the simulated RF shimmed B_1^+ map. For RF spokes pulse simulation, the same sinc RF pulses were employed, but with a modulation of the overall amplitude and phase of the pulse for each channel, where the static RF shimming was viewed as a single spoke at the origin of excitation k -space.

3.4. RF shim approach

In this study, the CP mode is referred to as 1-channel Tx. The CP mode or 1-channel Tx was calculated from the phases of the B_1^+ maps such that identical phase of the excitation pattern of all channels in the coil center led to constructive interference. The excitation voltage was identical for each Tx channel. This mimics the behavior of a quadrature birdcage coil, splitting the geometric phase by $2\pi/c$ in a c-port cylindrically symmetric coil [80].

The B_1^+ maps of 8 individual transmit channels were acquired with CP phase (phases were experimentally adjusted to match a CP solution) using TFL sequence as mentioned in “ B_1^+ mapping section”. Once 8 individual Tx channel B_1^+ maps were

acquired for multi slices, RF shimming experiments were performed by applying following methods.

3.4.1. Global and slice-selective RF shimming

In this approach, five different methods were compared: CP mode, global RF shimming, slice selective RF shimming, 2-spokes global shimming and 2-spokes slice selective shimming. As 2D B_1^+ maps were acquired over the brain volume, B_1^+ shim solutions or spokes could be calculated over ROI. To investigate variations in homogeneity and RF power compared to CP mode, the B_1^+ shims were calculated (i) over seven individual slices (slice-selective RF shimming method), and (ii) over the whole slice stack ($64 \times 64 \times 7$) (global RF shimming method).

To attain global shim method, only eight complex shim solutions were optimized through MLS algorithm and applied to all 8 individual coil elements. The amplitudes were scaled so that the mean flip angle (FA) of whole volume reached to the desired FA (90°). For slice-selective RF shimming, the amplitudes and phases were calculated for individual slices and then the amplitude of each slice was scaled so that the mean FA of each slice reached to desired FA (90°), which gives desired mean FA (90°) for whole slice stack. To simplify the presentation of results, this 90th percentile was scaled to a nominal value of 1.0 in the B_1^+ maps, which was then used to compare against global worst-case SAR.

The experiments using both RF shimming methods were performed in two different ways. The term λ in equation (3.4) can be used as a regularization term to control trade-off between homogeneity and RF power. With the use of λ , first the homogeneity of whole volume was adjusted to identical level and RF-power was calculated, and secondly, the RF-power was adjusted to identical level and homogeneity was calculated. Homogeneity and RF-power of B_1^+ maps were calculated for whole slice stack.

3.4.2. RF-shimming on higher number of Tx channel

In the case of 1-channel Tx, an identical RF-amplitude was applied for the whole slice stack in global shimming or for individual slices in slice-selective shimming, with CP phases, scaled to reach the desired mean FA over the target region.

The 8 individual Tx channel B_1^+ maps were acquired for multi slices in brain region. Using these B_1^+ maps of 8 individual coils, RF shimming adjustments were performed with 2-, 4-, and 8- coil combinations. A 2-channel Tx system was mimicked by complex summing of the four adjacent coil profiles after CP phase adjustment to form a virtual single coil element. The remaining four adjacent coil elements were summed similarly to form the second coil element. RF-shimming was then performed as in a 2-channel Tx situation. Similarly, a 4-channel Tx system was designed with complex summing of two adjacent coil elements and RF shimming experiments were performed on the resulting four-channel transmit system. For the 8-channel Tx system, all Tx channels operated

individually for RF shimming. The schematic of summing coil and generating 2- and 4-channel Tx system from 8-channel Tx system can be seen in Figure 7.

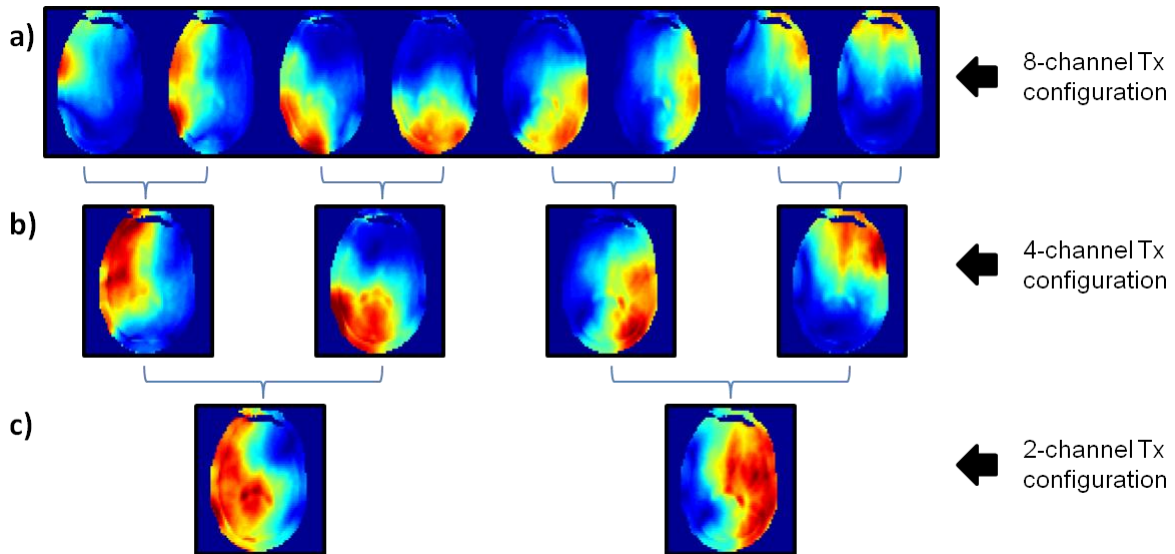


Figure 7: shows the design of different number of Tx channel configuration from 8 individual Tx channel B_1^+ maps. **a)** shows 8 independent B_1^+ maps, **b)** shows 4-Tx channel B_1^+ maps by summing B_1^+ maps of 2 adjacent Tx channel and **c)** shows 2-Tx channel configuration B_1^+ maps by summing 4 adjacent Tx channel B_1^+ maps.

Two quantitative studies were performed. The regularization term λ in Equation (3.4) was used to control the tradeoff between homogeneity and RF-power. In the first study, the RF-power of the 2-, 4- and 8-channel Tx was adjusted to be identical to that of the 1-channel Tx system, and the variation in homogeneity for all Tx configurations was analyzed. In the second study, the homogeneity was adjusted to be identical to that of the 1-channel Tx system, and the reduction in RF-power for all Tx configurations was

analyzed. These techniques were performed with the slice-selective and global RF shimming methods.

3.5. RF shim setting implementation

The Root Magnitude Mean Square Error (RMMSE) method was used to assess the homogeneity of the B_1^+ maps. The first term of equation 3.4 was used to calculate the deviation of the experimental B_1^+ map from the target (m), as shown in equation 3.5. In this study the target pattern m was a homogeneous vector.

Equation 3.5:

$$RMMSE = \sqrt{\| |Ab| - m \|^2}$$

The mean value of B_1^+ map was used as the value of target (m) in equation (3.5) for calculating RMMSE from the simulation and experimental data, in order to make a fair comparison between both results. The RMMSE value calculated from equation (3.5) was divided by the mean value of B_1^+ maps. An ideal B_1^+ field distribution would have an RMMSE of zero. The RF power in presented work is reported as the sum of squares of RF pulse amplitudes for all channels over all slices in the excited volume. This is a moderated method, which adopts the idea that all transmitted power contributes to RF-power.

The magnitude least square algorithm, implemented in MATLAB on a desktop PC, calculated all the complex coil weights for each particular slice and automatically transferred these to the MR system console. The TFL sequence was modified so that once the complex weights for individual coils and slices were calculated, the sequence

would use these shim solutions for suitable coil elements and the slices to perform real time shimming during the measurements.

Simulated B_1^+ maps were obtained for each optimized shim setting to allow comparison between the simulated and measured B_1^+ distributions. Based on simulated B_1^+ maps, the RF excitation pulses for each measurement were scaled so that the mean FA of experimental results was 90° (nominal), the same as the target FA for all measurements. For slice shimming, the mean FA of each slice was adjusted to nominal FA; for the global shimming, the mean FA of the whole slice stack was set to nominal FA. A full examination, consisting of B_1^+ mapping, RF shim calculation, and acquisition of images for all channel combinations, could be performed within 50 minutes.

The RF-power, in this dissertation, is reported as the sum of squares of RF pulse peak amplitudes for all transmit channels. This is a conservative approach that assumes all forward power contributes to global SAR.

3.6. Imaging sequence protocol

To demonstrate RF shimming performance in anatomical imaging, GRE images, T2-weighted 2D Turbo-Spin-Echo (TSE) images and T1-weighted Spin-Echo (SE) images were acquired. The imaging parameters for the GRE sequence were: 230×230 mm, matrix size: 256×256 , slice thickness: 5 mm, TR/TE: 50/2.27 ms and FA = 15° . The imaging parameters for the T2w TSE were FOV: 230×230 mm, matrix size: 256×256 ,

MATERIALS AND METHODS

slice thickness: 5 mm, TR/TE: 5 s/50 ms, echo spacing: 9.93 ms, echoes per train: 9, center echo: 5, bandwidth: 217 Hz/Px. Imaging parameters for T1w SE were FOV: 230 × 230 mm, matrix size: 256 × 256, slice thickness: 5 mm, TR/TE: 700 ms/9.8 ms, bandwidth: 217 Hz/Px.

4

Results

The rapid quantitative B_1^+ mapping method using Turbo-FLASH, as presented in the previous section was used to acquire B_1^+ profiles of independent Tx channel at 7T in *in-vivo* and the individual Tx channel B_1^+ profile were presented in Figure 5 (in the previous chapter). These individual Tx channel B_1^+ maps were fed in to magnitude least square equation to optimize amplitude and phase values or to design spokes pulses for individual Tx channel to homogenize B_1^+ field. All RF shimming experiments were performed on five healthy volunteers and had the aim of improved imaging.

4.1. Global and slice-selective RF shimming

Initially the RF shimming was applied to single slice and compared it with CP B_1^+ maps. These measured CP and static RF shimmed B_1^+ maps from single volunteer are shown in Figure 8 a) and b) respectively. The B_1^+ maps in Figure 8 were acquired in: i) transverse orientation using Body coil, ii) coronal orientation using Body coil, iii) transverse orientation using Head coil and iv) sagittal orientation using Head coil.

RESULTS

Shimming the B_1^+ field with static RF shim showed improvements in homogeneity of 38%, 40%, 52% and 50% from i) to iv) respectively, in comparison to CP B_1^+ maps.

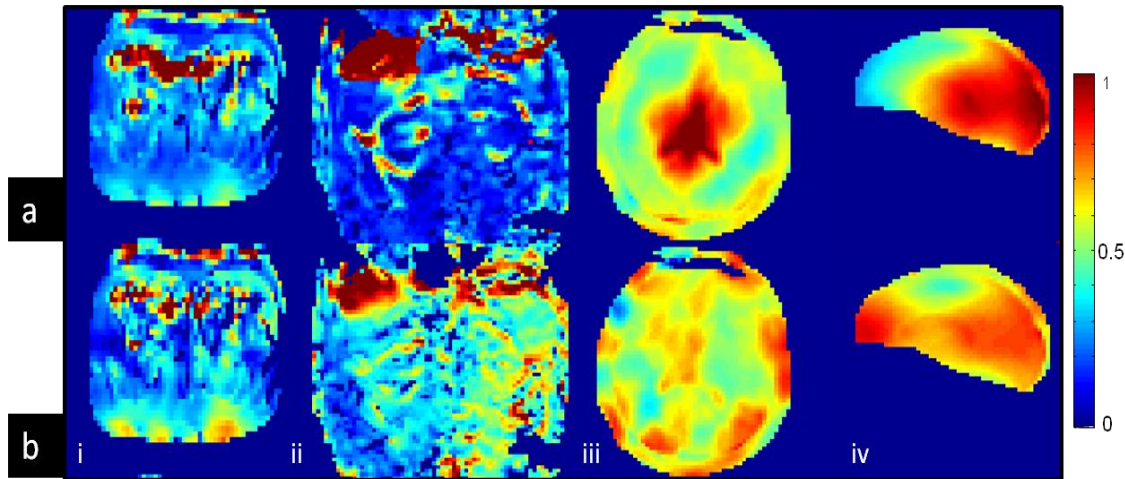


Figure 8: a) and b) shows B_1^+ maps acquired in CP mode and with static RF shimming method respectively: i) transverse orientation using Body coil, ii) coronal orientation using Body coil, iii) transverse orientation using Head coil and iv) sagittal orientation using Head coil.

Anatomical images were also acquired in CP and static RF shim situations. Figure 9 depicts corresponding anatomical images respectively. The intensity variation behavior of anatomical images was similar as measured B_1^+ maps.

RESULTS

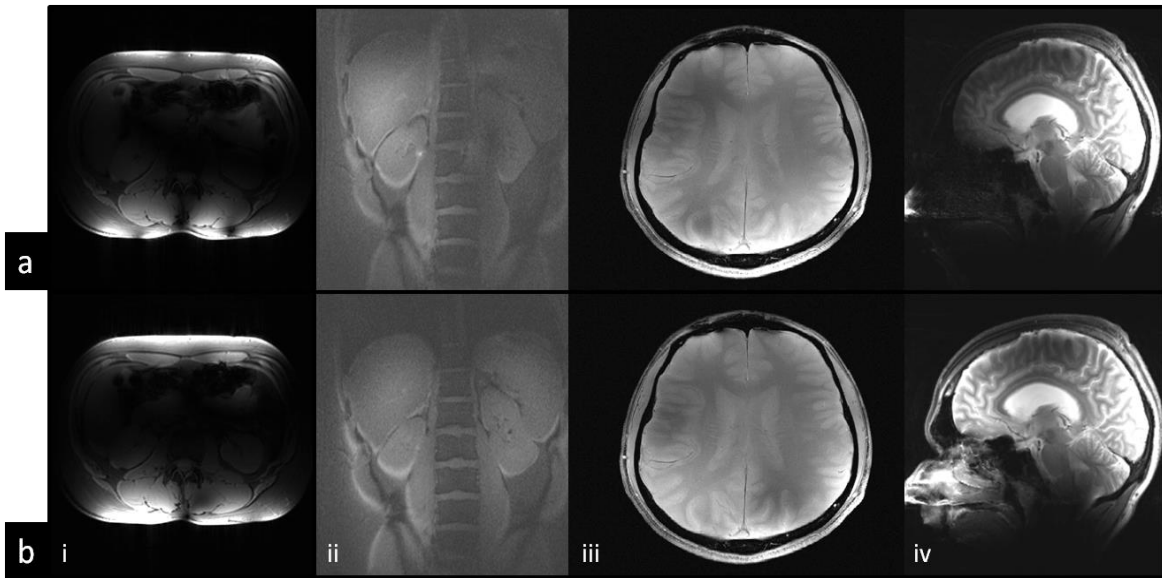


Figure 9: represents anatomical image of **a)** CP mode and **b)** RF shimmed. These images are acquired in same scenario as shown in figure 9 respectively. **i)** transverse orientation using Body coil, **ii)** coronal orientation using Body coil, **iii)** transverse orientation using Head coil and **iv)** sagittal orientation using Head coil.

The different RF shimming techniques were then attempted on brain volume, to find the best RF shimming fidelity to homogenize the volume in brain region with reduced RF power. A total of five different shimming methods were applied: 1) CP, 2) global static RF shimming, 3) slice-selective static RF shimming, 4) global 2-spokes pulse and 5) slice selective 2-spokes pulses. The results from single volunteer are presented in Figure 10 and 11. The transversal oriented measured B_1^+ maps are presented in Figure 10 a) and the RMMSE values are presented in Figure 10 b). In similar manner, the multi-slice B_1^+ maps and RMMSE values for sagittal orientation are presented in Figure

RESULTS

11 a) and b) respectively. The CP, global and static RF shimmed B_1^+ maps were acquired with identical RF-power for excited slice stack. The RMMSE values for transversal oriented B_1^+ maps are 0.9%, 0.65%, 0.57% and 0.45% (drop in RMMSE is 10%, 35%, 43% and 55% compared to CP B_1^+ map) for global, slice selective, global 2 spokes and slice selective 2 spokes RF shimming respectively. The RMMSE for sagittal oriented B_1^+ is 0.82%, 0.46%, 0.32% and 0.29% (drop in RMMSE is 18%, 54%, 68% and 71% compared to CP B_1^+ map) for global, slice selective, global 2 spokes and slice selective 2 spokes RF shimming compared to CP B_1^+ maps respectively.

The RMMSE values of B_1^+ maps for transversal and sagittal orientations indicate that the CP mode has least homogeneity compared to other presented shimming methods. When shimming the whole volume globally, the RMMSE decreased. However, the individual slice shimming method shows better homogeneity, compared to CP and global shimming methods. The homogeneity could further improve when global 2-spokes and slice-selective 2-spokes pulses are applied to slice stack.

RESULTS

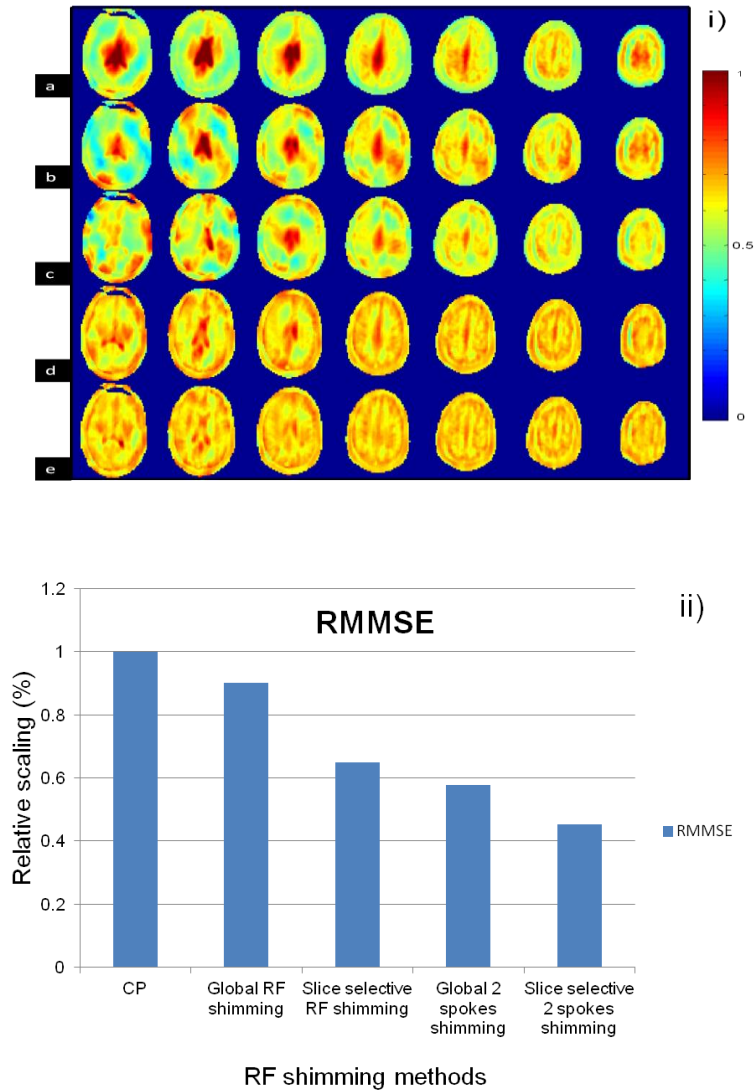


Figure 10: i) Represents B₁⁺ maps for a transversal stack of slices. a) CP-mode, b) Global shimming, c) Slice-selective shimming, d) Global 2-spokes shimming and e) Slice-selective 2-spokes shimming. ii) shows corresponding RMMSE values of B₁⁺ maps. The RMMSE was summed over whole volume.

RESULTS

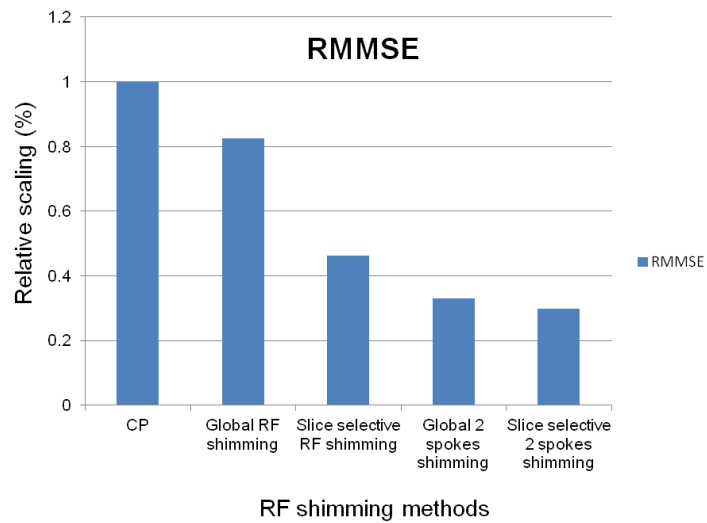
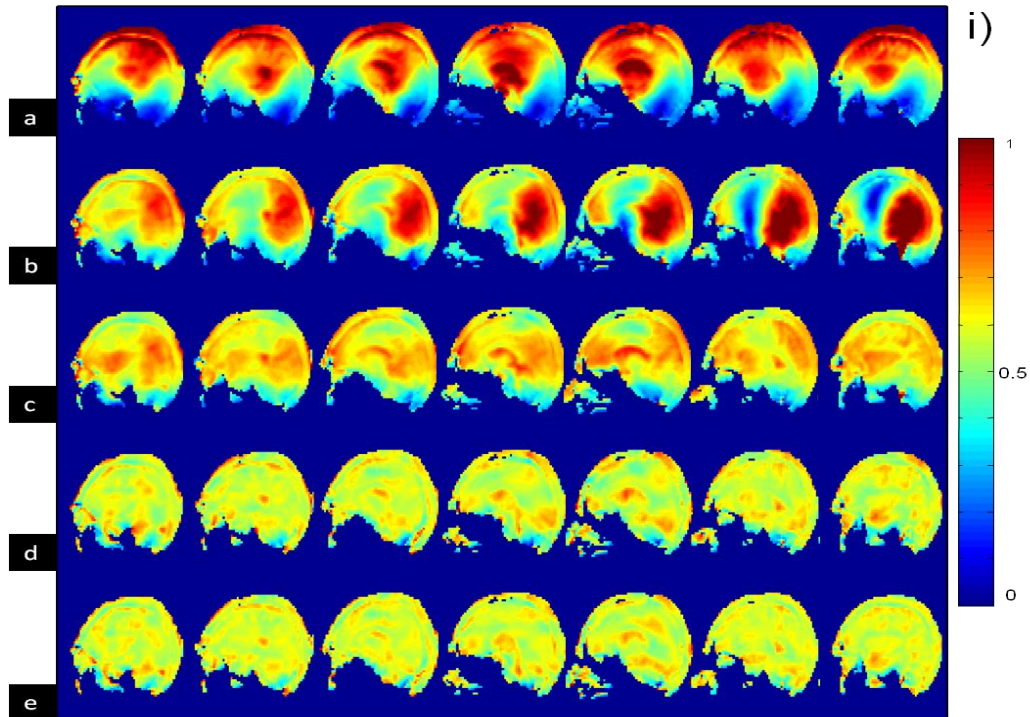


Figure 11: i) Represents shim solutions for a sagittal stack of slices. a) CP-mode, b) Global shimming, c) Slice-selective shimming, d) Global 2-spokes shimming and e) Slice-selective 2-spokes shimming. ii) shows corresponding RMMSE values of B_1^+ maps. The RMMSE was summed over whole volume.

RESULTS

The variations in homogeneity are more visible in the sagittal orientation than transversal orientation, because the coil is transversal oriented. In the transversal orientation, all Tx channels contributed equally to the object. However, for sagittal orientation, each Tx channel contribution is different depending on slice location. The slice that is closed to Tx channel has higher influence of neighboring Tx channel than opposite Tx channel.

Anatomical images were also acquired with CP and different shim settings. Figure 12 shows multi slice brain images acquired with GRE sequence on single volunteers. Figure 12. Images i) ii) & iii) are acquired with CP mode, global RF shimming and slice selective RF shimming. The signal variations behave similarly to B_1^+ profile shown in figure 11.

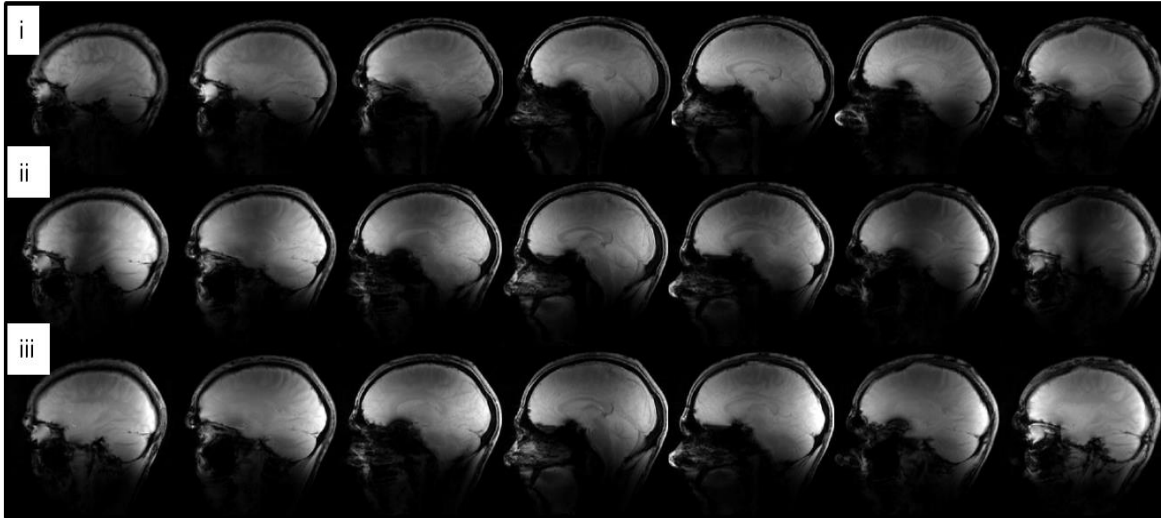


Figure 12: i), ii) & iii) shows multi slice brain images acquired with GRE sequence in CP mode, global shim and slice selective shimming methods respectively.

4.2. Higher number of Tx channels

The RMMSE and RF-power were further investigated with different number of Tx channel combinations (1-channel Tx to 2-, 4- and 8-channel Tx) using global RF shimming and slice-selective RF shimming methods. The effects of using more Tx channels in a single volunteer can be seen in Figure 13. This is a comparison study for the best (lowest RMMSE) possible homogeneity which can be achieved with 1-, 2-, 4-, and 8-channel Tx using static RF shimming (Figure 13.i, a-d) with identical RF-power for each of the Tx channel configurations and using 2- and 3- spokes (Figure 13. I, e-f). The mean value of all maps was scaled to 1. The magnitude profiles resulting from the 2-, 4-, and 8-channel Tx configuration shows drop in RMMSE of 11%, 27%, and 45% in

RESULTS

single volunteers respectively, compared to the 1-channel Tx. For static RF shimming, the 8-channel Tx design shows significantly reduced RMMSE compared with 1-, 2- or 4-channel Tx shim design.

The RF pulses with 3- and 2-spokes were applied to the 2- and 4-channel Tx configurations respectively, the homogeneity was similar to that of the 8-channel Tx system with static RF shimming, which is equivalent to a 1-spoke pulse. The number of spokes for 2- and 4-channel Tx was determined to achieve RMMSE similar to that of a static-shimmed 8-channel Tx system.

Figure 13. ii) and iii) depicts representative slices from the T2w TSE and the T1w SE image series, acquired with the 1-, 2-, 4-, and 8-channel Tx static shim solutions with identical RF-power. The intensity variations resemble the spatial patterns in the measured B_1^+ maps (Figure 13. I, a-d). For the T1w and T2w images, the perceived image homogeneity increases with increasing number of channels for the given brain anatomy. These images were not corrected for receive coil sensitivities.

RESULTS

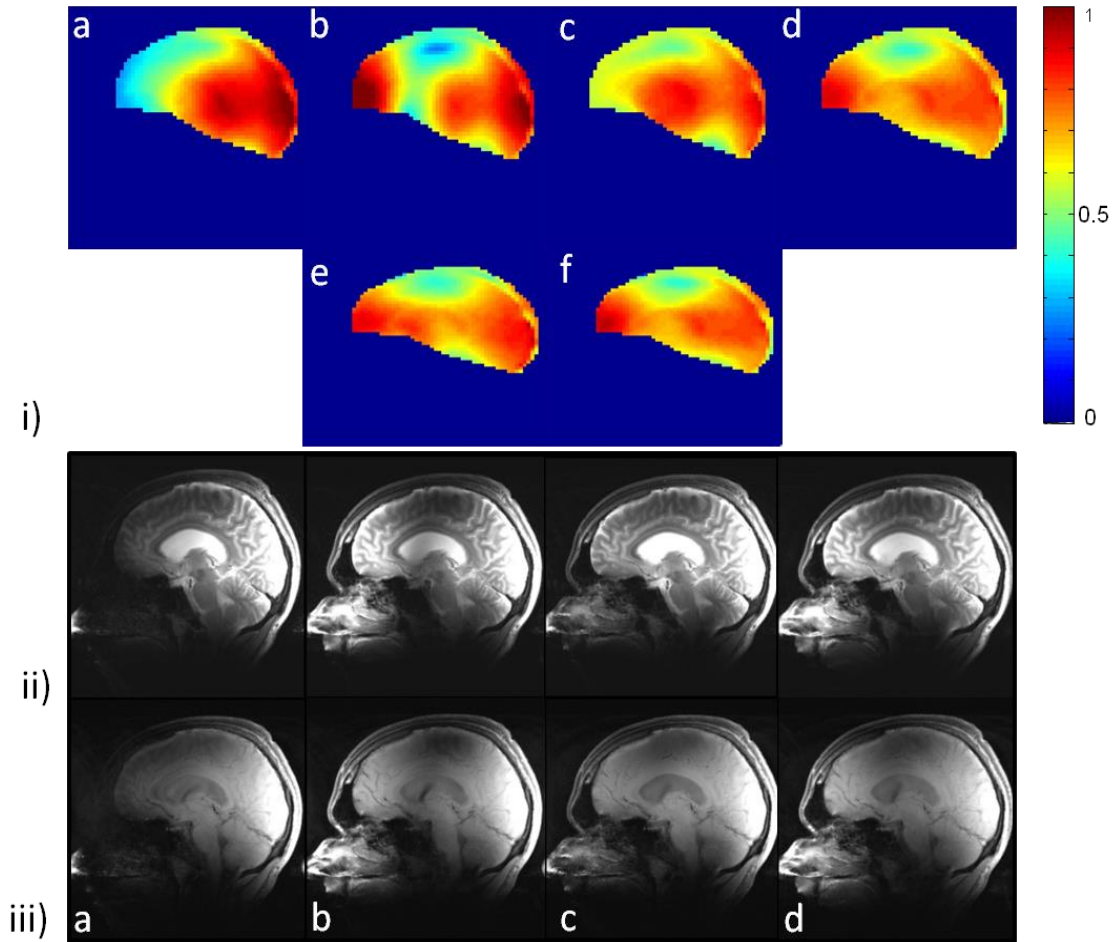


Figure 13: **(i)** shows experimented RF shimmed B_1^+ maps acquired in sagittal orientation: **(a)** 1-channel Tx, **(b)** static RF shimmed with 2-channel Tx, **(c)** static RF shimmed with 4-channel Tx, **(d)** static RF shimmed with 8-channel Tx **(e)** 3 spokes with 2-channel Tx and **(f)** 2-spokes with 4-channel Tx configurations. **(ii) a-d** shows T2w TSE and **(iii) a-d** shows T1w SE images, acquired by performing static RF-shimming with 1-, 2-, 4- and 8-channel Tx configurations respectively.

A multi slice experiment was carried out to investigate B_1^+ homogeneity and RF-power relation in brain volume. Figure 14.i) a) to d) shows the B_1^+ maps acquired in 1-, 2-, 4-

RESULTS

and 8-channel Tx configurations respectively. These B_1^+ maps are acquired with identical RF-power for all Tx channel configurations. Figure 14.ii) shows the RMMSE value of Tx channel configurations. With increasing the Tx channel configuration from 2-, 4- and 8-channel Tx the RMMSE value reduces 30%, 45% and 55% compare to 1-channel Tx system respectively.

RESULTS

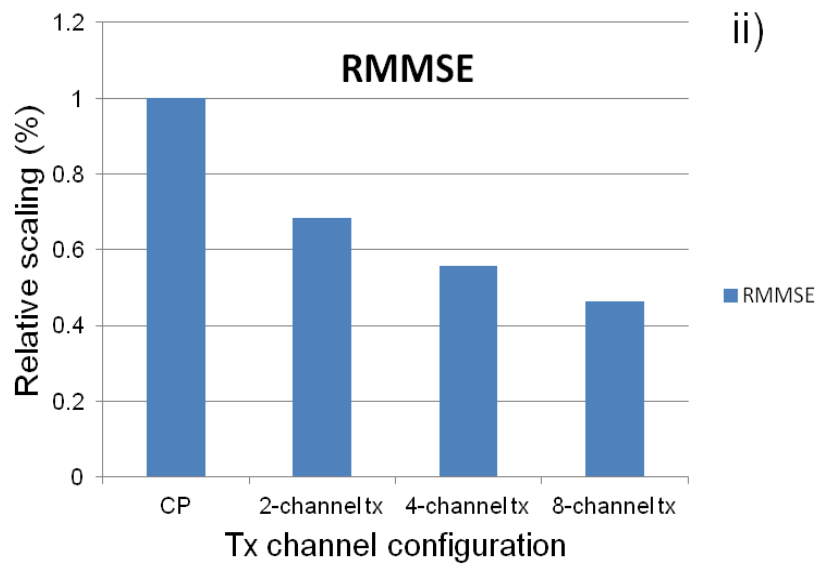
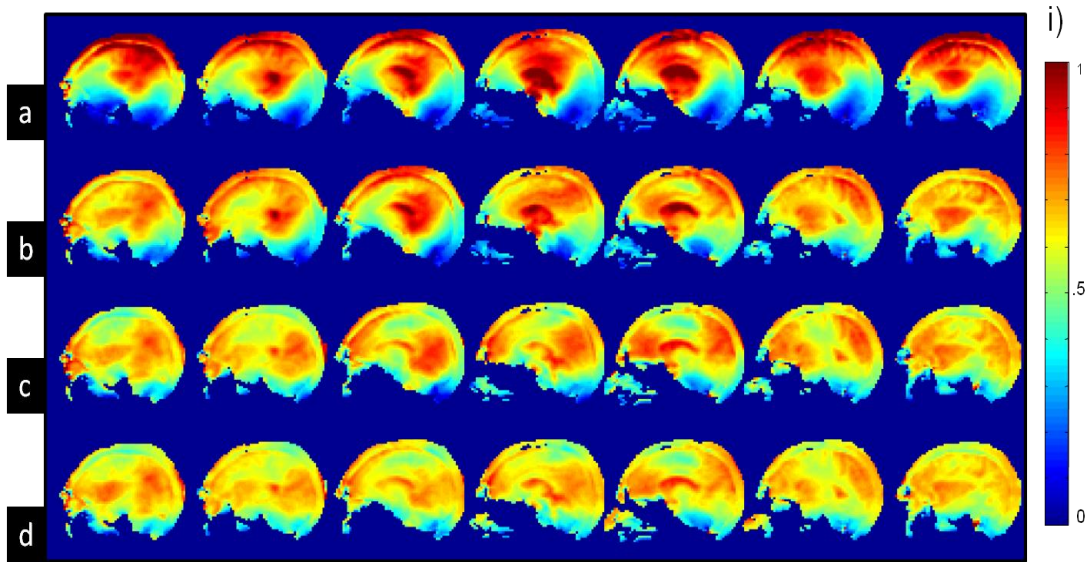


Figure 14: **i)** Shows static RF shimmed B_1^+ maps acquired in sagittal orientation: **(a)** 1-channel Tx, **(b)** 2-channel Tx, **(c)** 4-channel Tx and **(d)** 8-channel Tx configurations. **ii)** shows corresponding RMMSE values of B_1^+ maps. The RMMSE was summed over whole volume.

4.3. Quantitative studies

The approaches mentioned previously were applied together on five volunteers. Initially the different number of Tx configuration and RF shimming methods were examined with identical RF power and change in homogeneity was investigated and after that homogeneity was adjusted to identical and the variation in RF-power was investigated. Figure 15 represents study of the variation in homogeneity at identical average RF-power (Figure 15.a) and the reduction in RF-power at identical average homogeneity (Figure 15.b) for the 1-, 2-, 4- and 8-channel Tx configurations over all slices and five subjects. These figures include findings from slice-selective and global RF shimming (normalized to the 1-channel Tx mode of global RF shimming) which depict the average values for different subjects, and the error bar represents the standard error over subjects. Both figures quantify the homogeneity by means of RMMSE of the calculated B_1^+ field, and the RF-power is computed as the sum of squares of RF pulse amplitudes for all transmit channels. When slice-selective RF shimming was used instead of global RF shimming, and with an increasing number of transmit channels from 1-channel Tx to 8-channel Tx, the B_1^+ field distribution in the brain at 7T became more homogenous, and when all shim solutions had approximately identical homogeneity (Figure 15. ii), the RF-power progressively decreased with increasing the numbers of Tx channels.

RESULTS

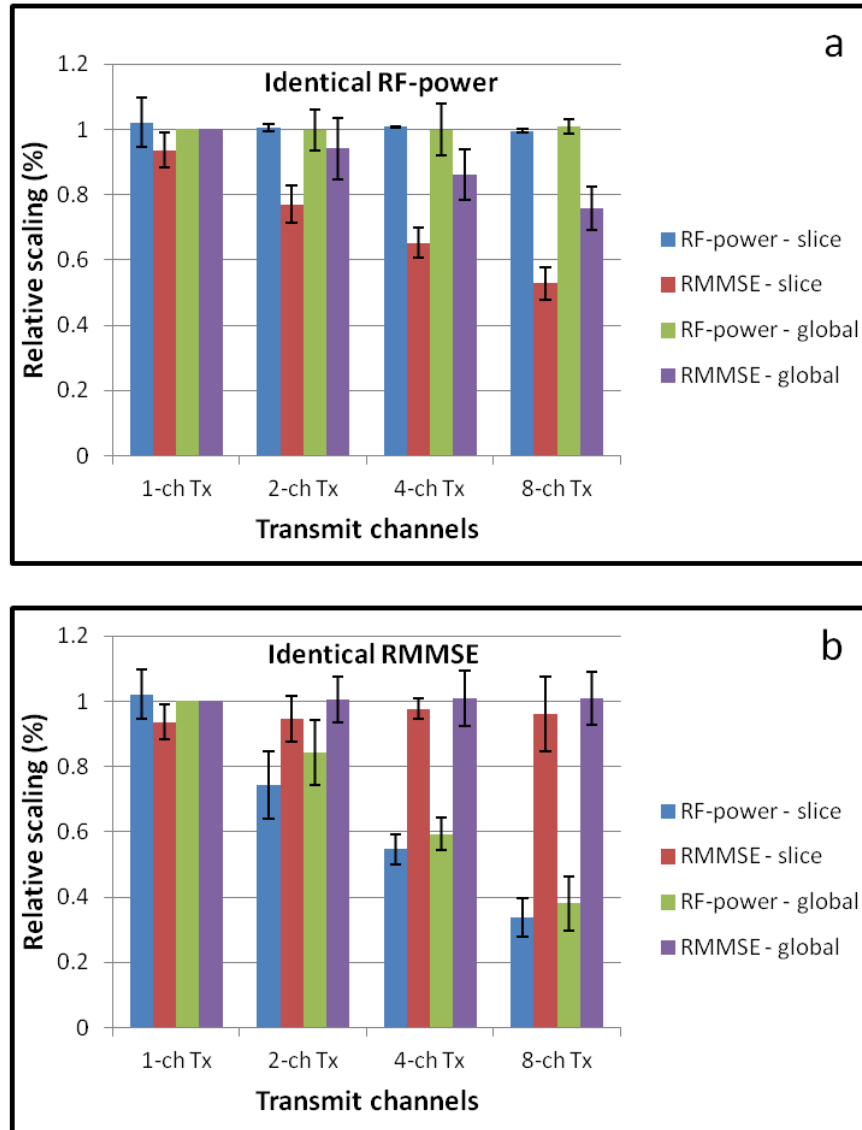


Figure 15: RF-power and RMMSE, averaged over the volume, for the two shimming methods: slice-selective RF shimming and global RF shimming, for 1, 2, 4, and 8 Tx channels. Chart **a)** represents findings when the RF-power was identical for all configurations, and chart **b)** shows findings when the RMMSE was identical for all configurations. All values have been normalized to the 1-channel Tx mode of the global RF shimming. Error bars represent the standard error over the subjects.

RESULTS

Figure 16 represents changes in the RF-power and RMMSE with slice location for all Tx channel configurations for five subjects. Results with identical RF-power and identical RMMSE for all channels are represented in Figure 16a-d and 16e-h respectively. All graphs are normalized to the center slice of the 1-channel Tx global mode. For slice-selective RF shimming, each slice was shimmed individually, so the RF-power in Figure 16 a) changes with slice location, and for global RF shimming, the whole slice stack was shimmed so that Figure 16 b) depicts the same RF-power for the whole slice stack. For comparison, the RMMSE and RF-power were averaged over the entire slice stack for slice-selective and global RF shimming.

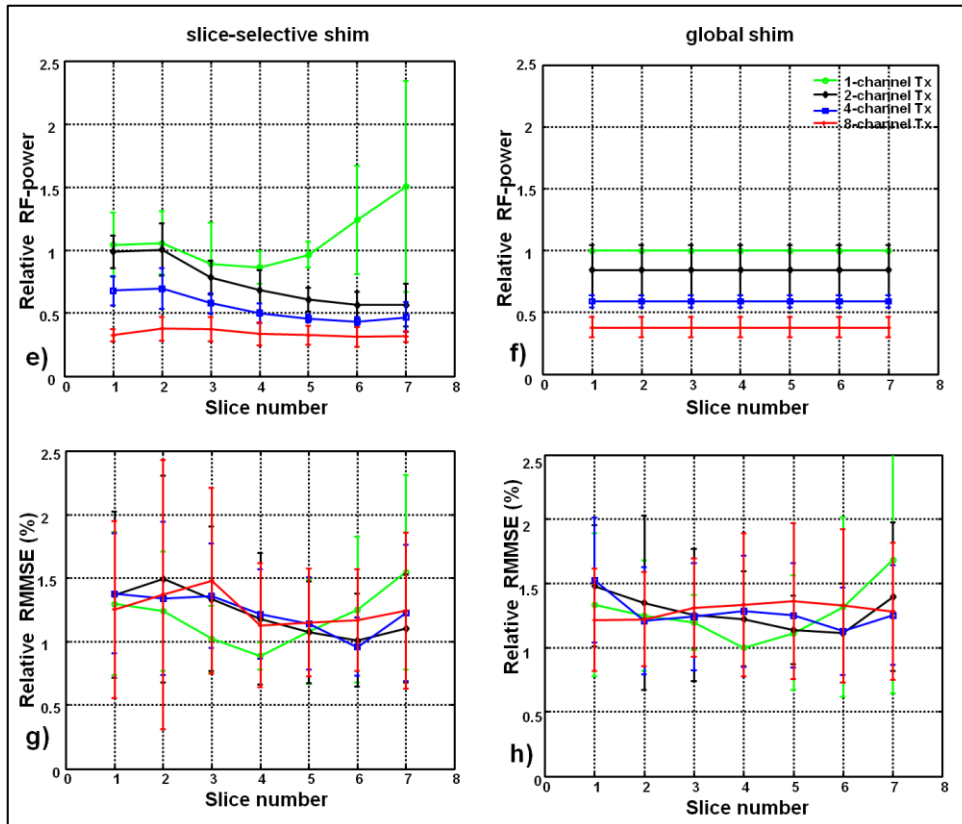
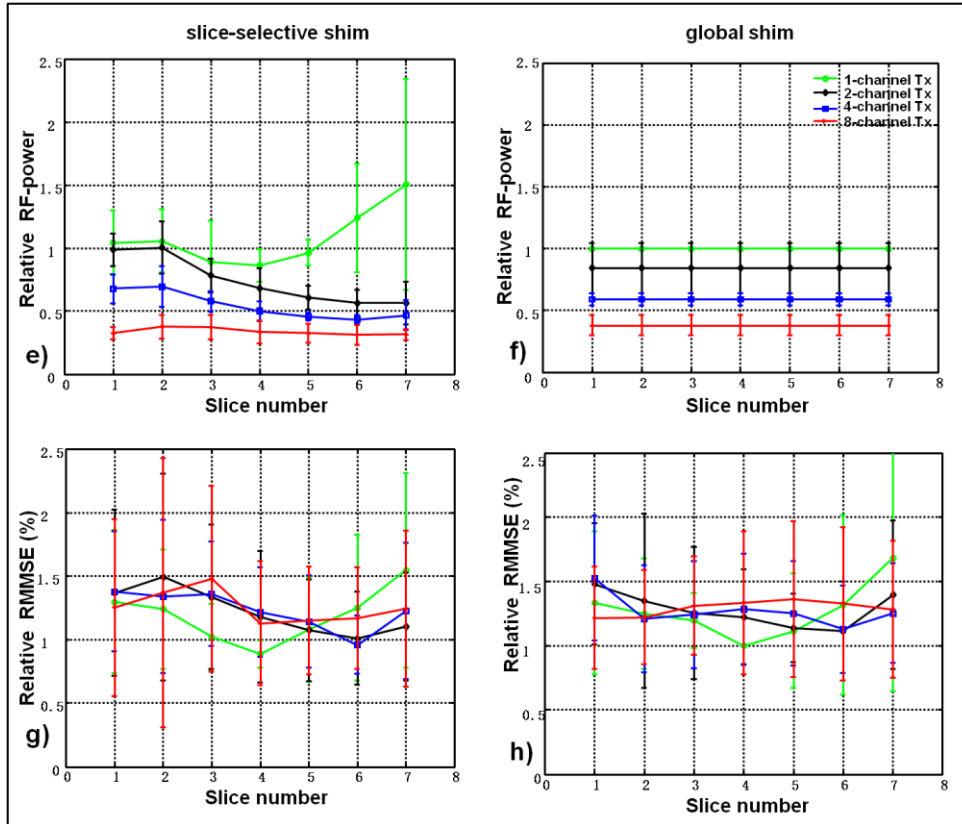
The 1-channel Tx global mode displays an inferior performance compared with the slice-selective RF shimming method and other Tx channel configurations, with RMMSE in B_1^+ being nearly 40% (RMMSE of an ideal B_1^+ field would be 0%), and the 1-channel Tx slice-selective mode has an RMMSE of 36%. Table 1 shows the mean value of RMMSE and RF-power over the slice stack presented in figure 16. With constant RF-power and slice-selective RF shimming, the RMMSE for 2-, 4-, and 8-channel Tx when compared with 1-channel Tx (RMMSE of 1-channel Tx scaled to 1%) was $0.82 \pm 0.08\%$, $0.7 \pm 0.05\%$ and $0.56 \pm 0.07\%$ (reduction in RMMSE was $18 \pm 8\%$, $30 \pm 5\%$ and $44 \pm 7\%$) respectively, whereas with a constant RMMSE and slice-selective RF shimming, the RF-power (RF-power of 1-channel Tx scaled to 1%) for 2-, 4-, and 8-channels Tx was $0.69 \pm 0.05\%$, $0.51 \pm 0.07\%$, and $0.31 \pm 0.07\%$ (reduction in RF-power was $31 \pm 5\%$, $49 \pm 7\%$ and $69 \pm 7\%$) respectively, compared with 1-channel Tx. In this scenario, the performance of global RF shimming was inferior compared with the slice-selective

RESULTS

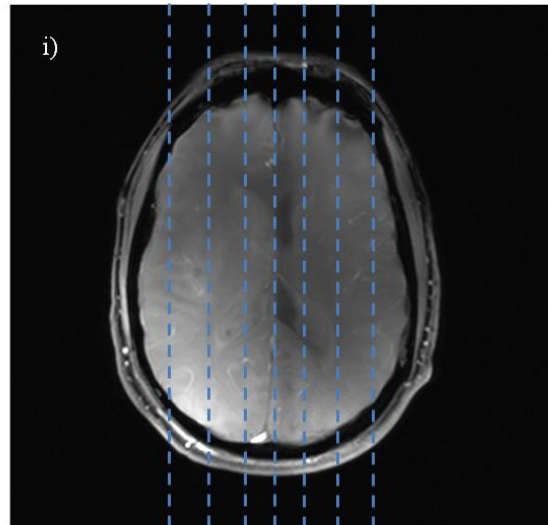
method. For identical RF-power, the RMMSE for 2-, 4-, and 8-channels Tx compared to 1-channel Tx was $0.94\pm 0.06\%$, $0.86\pm 0.05\%$ and $0.76\pm 0.02\%$ (reduction in RMMSE was $6\pm 6\%$, $14\pm 5\%$ and $24\pm 5\%$) respectively and the RF-power for identical RMMSE for 2-, 4-, and 8-channels Tx compared with 1-channel Tx excitation was $0.84\pm 0.05\%$, $0.59\pm 0.03\%$, and $0.38\pm 0.05\%$ (reduction in RF-power was $16\pm 5\%$, $41\pm 3\%$ and $62\pm 5\%$) respectively.

The slice-selective RF shimming method with 8-channel Tx showed marked improvements over global RF shimming and fewer Tx channels. In the case of slice selective shimming and global shimming, same value of λ was used. In the case of identical RF-power or RMMSE, the graphs depict variation for different slice (e.g. 16 a, g and h), but the mean value of RF-power or RMMSE is 1.

RESULTS



RESULTS



Approximate slice locations

Figure 16: The changes in RF-power and RMMSE (relative to center slice of 1-channel Tx global mode) of B_1^+ with slice locations. **(a-d)** depicts findings for identical value of RF-power for all Tx channel configurations, and **(e-h)** shows findings for identical value of RMMSE for all Tx channel configurations. **(i)** Localizer image shows approximated sagittal slice locations of human volunteers.

RESULTS

Shimming methods	RMMSE/R F-power	1-channel Tx	2-channel Tx	4-channel Tx	8-channel Tx
Slice-selective shim	RMMSE for Identical RF-power	1%	0.82 ± 0.08%	0.7 ± 0.05%	0.56 ± 0.07%
	RF-power for Identical RMMSE	1%	0.69 ± 0.05%	0.51 ± 0.07%	0.31 ± 0.07%
Global RF shim	RMMSE Identical RF-power	1%	0.94 ± 0.06%	0.86 ± 0.05%	0.76 ± 0.02%
	RF-power Identical RMMSE	1%	0.84 ± 0.05%	0.59 ± 0.03%	0.38 ± 0.05%

Table 1: The table shows the mean value of RMMSE and RF-power over the slice stack presented in figure 18. All the values were normalized to 1-channel Tx mode. RF-power and RMMSE of 1-channel Tx scaled to 1%.

Figure 17 portrays the tradeoff between RF-power and RMMSE when various values of λ were used for the slice-selective and global RF shimming methods with 1-, 2-, 4- and 8-channel Tx configurations. It shows the inverse relation between RF-power and RMMSE. Figure 17 a) shows L-curve for transverse oriented volume and b) shows L-curve for sagittal oriented volume. These data are calculated for multiple volunteers and the only mean values over the volume are plotted as a curve in order to prevent overlapping of curves which could further lead to complexity of the graph. Imaging experiments were performed for equal RF-power for all Tx channel configurations, where measurable differences in B_1^+ were achieved. In order to keep the duration of the

RESULTS

examination suitable for the human subjects, the other solutions of λ were not used for imaging. Therefore, the plots presented in Figure 17 are based on simulations.

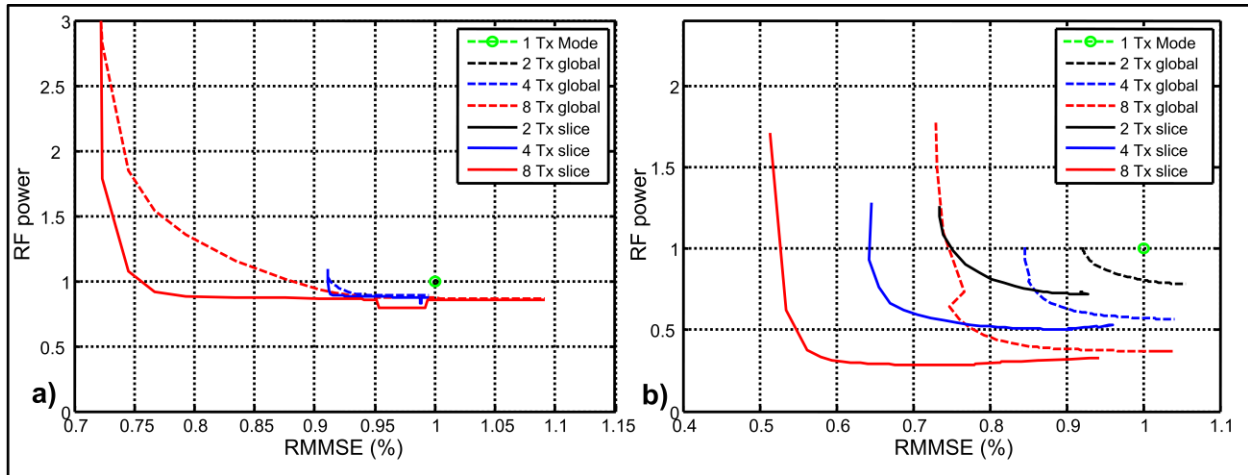


Figure 17: Tradeoffs between relative RF-power and RMMSE for 1-, 2-, 4-, and 8-channel Tx configurations for slice-selective and global RF shimming methods. Each curve is generated by performing the RF shimming calculation for multiple values of the regularization λ parameter. **a)** is L-curve for transverse oriented volume and **b)** is sagittal oriented volume. Different colors represent different numbers of Tx channels.

5

Discussion

The use of high field strengths in MRI has many benefits such as better contrast images and good signal to noise ratios. However, in typical 1-channel Tx systems using standard elliptical 'birdcage' coils, there is considerable B_1^+ inhomogeneity and RF-power requirement at high field strengths. Therefore, there is a need for more sophisticated shimming methods or different Tx coil geometries in order to improve B_1^+ homogeneity and/or reduce RF-power over the brain region. At high field strengths, the use of 8 Tx channels and slice-selective RF shimming leads to higher fidelity (through reduction in inhomogeneity and RF-power) than the single-channel Tx mode.

In this work, RF shimming has been used with an increasing number of channels (2, 4 and 8), to add additional degrees of freedom to the B_1^+ behavior. Considerable improvements in B_1^+ uniformity and/or reduction in RF-power were observed for 2- or 4-channel Tx, when compared with the 1-channel Tx mode. However, with 8 Tx channels, the improvement in B_1^+ uniformity and/or a reduction in RF-power was remarkable when compared with lower number of Tx channels (1-, 2-, or 4-channel Tx), clearly indicating that with increasing numbers of Tx channels, we can expect better performance. An

DISCUSSION

alternative of using higher number of Tx channel to homogenize B_1^+ field is designing RF spokes pulses at lower number of transmit channel system, as shown in Figure 10&11. However, long durations of the RF and the gradient pulses are a major technical limitation of spokes pulse excitation. The pulse durations are progressively longer with increasing shape complexity of the volume of interest. In general, RF pulses and gradient which follow practical amplitude and slew rate limitations (based on physiological parameters, not hardware limitations) and create complex patterns, are impracticably long. They are also prone to system imperfection and hence are not used in clinical applications. For example, slice selective excitations that use spokes trajectory to mitigate severe B_1^+ inhomogeneity can be very long. This is due to the large number of k_z spokes which are required on many k_x - k_y locations to create an in-plane excitation pattern that is sufficient to counteract the severe inhomogeneity. By using higher number of transmit channels, however, the duration of excitation pulses can be significantly shortened compared to the single-channel case.

Another approach towards improving B_1^+ behavior which is presented in this work, is the use of slice-selective RF shimming, in comparison with global RF shimming. In slice-selective RF shimming, reduction of RMMSE and RF-power in the slice stack was observed as each slice was shimmed and scaled up to the desired FA. This reduction in RF-power and RMMSE was more rapid in the slice-selective RF shimming method than in the global RF shimming method, for identical values of λ (Figure 17).

DISCUSSION

For 8-channel Tx system with slice selective shimming method for small values of λ , the reduction of RF-power is rapid with only minor increase in RMMSE compared to other Tx channel configurations (as shown in Figure 17). With greater values of λ , RF-power reduction becomes negligible and RMMSE increases rapidly. Hence, choosing a specific value of λ in the least square equation at which RF-power reduction ceases to be significant and RMMSE begins to increase could be the efficient solution of λ for RF shimming compared to the standard fixed phase MR system at high field strength which has a major limitation with regards to RF-power. The reductions in RMMSE and RF-power for the slice-selective RF shimming method and for 2-, 4-, and 8-channel Tx configuration were 25%, 23% and 20% respectively compared to the global RF shimming method, for an efficient solution of λ . This RF-power reduction would beneficially increase allowable global SAR, which could in turn be used to increase FA, acquire more slices within a fixed TR or reduce TR. Such effects would be advantageous for sequences requiring higher RF-power, e.g. T1w SE, or for 3D imaging. Slice-selective RF shimming with 8 Tx channels for an efficient solution of λ could also be used in combination with other methods, like Transmit SENSE [79], selective excitation [81] or BOLD MRI of kidney [82,83]. Slice-selective RF shimming would also reduce magnetization transfer effects compared to global RF shimming as these effects depend on the B_1^+ field of neighboring slices.

One important observation was noted from the L-curve shown in Figure 17. Sagittal oriented slices showed more improvement in homogeneity and reduction in RF-power than the transversal oriented slices. This is because an axial oriented coil was used for

DISCUSSION

this study. In transversal excitation, the brain anatomy is visible in entire slice even though the CP mode is inhomogeneous. There is more control in axial slices as 8 elements effectively contribute. In sagittal slices only few elements vary. In imaging experiments using the improved methods presented in this thesis, the brain anatomy was more visible in sagittal oriented brain region as well as more homogeneous. In the 8-channel Tx system with slice selective method, sagittal volume shows 45% improvement in homogeneity and RF-power reduction compared to CP mode, while transversal volume shows 25% improvement under the same conditions, for efficient solution of λ .

In this work, it was attempted to balance B_1^+ homogeneity with total drive power, and derive a relation between them as an L-curve. Thus, this method affords flexibility in choosing a suitable operating point from the L-curve, depending on the situation. Constant power or constant homogeneity solutions were used in this study, but it is possible to select any point along the curves for a particular application. Different sequences have different levels of sensitivity to B_1^+ inhomogeneity, therefore suitable homogeneity-power tradeoffs can be selected for particular situations. For example, the T2w sequence employed here is fairly robust, so a lower power solution could be used to increase efficiency. For other parts of an examination that may be much more vulnerable to B_1^+ inhomogeneity, a different homogeneity-power tradeoff could be selected. Thus a flexible balancing of SAR load across a whole examination can be achieved. At the other extreme, if the total power is not a concern, then it is possible to

DISCUSSION

achieve highly homogeneous B_1^+ fields over a large (axial) field of view with a multi-transmit system at 7T, as shown in Figure 17.

Due to the unavailability of a suitable RF-power simulation model for the volunteers imaged for this study, the actual local RF-power values were not modeled. Hence, the imaging performance was restricted to 1/8 (12.5%) of the RF power limits of the same geometry standard single channel transmit and eight channel receive coil (Rapid Biomedical, Rimpar, Germany) to ensure subject safety for any possible constructive RF interference. For subject-specific estimation of the local SAR, it would be necessary to have personalized SAR models for each subject. These would represent the SAR more accurately if the regularization term in Equation 3.4 was replaced with a term based directly on a true SAR estimate. In a recent study by Homann et al. [84], shimming with an 8-channel coil, of a similar design to the one in this work, was investigated. It was found that substantial SAR reductions were possible by including a subject specific SAR model when determining shim settings.

The present work may suggest a systematic study of Tx coil array configurations with multiple elements arranged in all three spatial directions around the head [50,85], and future investigation of additional degrees of freedom which may result in further reduction in inhomogeneity. This study was performed using 8-channels Tx, and the results indicate that RF shimming with more than 8-channels Tx could alleviate B_1^+ inhomogeneity even more effectively. It is expected that the presented method for slice-

DISCUSSION

selective excitation with 8-Tx will also work effectively for coronal and generally oblique scan planes, beyond the axial and sagittal demonstrations in this work.

6

Conclusion

The parallel transmission method was used in this study to create RF excitation that mitigated B_1^+ inhomogeneity while satisfying the constraint of sufficiently low RF-power, to make it suitable for practical clinical applications. Novel RF shimming methods were used in this dissertation with excellent excitation control and lower RF-power requirement. A slice by slice shimming strategy with 8-channel Tx configuration was implemented in 7T high field scanners with an efficient value of λ to demonstrate the ability of this method to achieve high-fidelity B_1^+ mitigation. It was observed that parallel transmit hardware is at least 25% more efficient compared to the standard MR systems which are used universally. In this work, the maximum number of Tx channels used was 8. Hypothetically, using a greater number of Tx channels with an appropriate coil array can provide superior performance in the brain region at high field strength.

References

1. Hollingworth, W.; Todd, C.J.; Bell, M.I.; Arafat, Q.; Girling, S.; Karia, K.R.; Dixon, A.K. The diagnostic and therapeutic impact of MRI: an observational multi-centre study. *Clin Radiol* 2000, *55*, 825–831.
2. Hoenig, K.; Kuhl, C.K.; Scheef, L. Functional 3.0-T MR assessment of higher cognitive function: are there advantages over 1.5-T imaging? *Radiology* 2005, *234*, 860–868.
3. Kuhl, C.K.; Textor, J.; Gieseke, J.; Falkenhausen, M. von; Gernert, S.; Urbach, H.; Schild, H.H. Acute and subacute ischemic stroke at high-field-strength (3.0-T) diffusion-weighted MR imaging: intraindividual comparative study. *Radiology* 2005, *234*, 509–516.
4. Manka, C.; Traber, F.; Gieseke, J.; Schild, H.H.; Kuhl, C.K. Three-dimensional dynamic susceptibility-weighted perfusion MR imaging at 3.0 T: feasibility and contrast agent dose. *Radiology* 2005, *234*, 869–877.
5. Saupe, N.; Prussmann, K.P.; Luechinger, R.; Bosiger, P.; Marincek, B.; Weishaupt, D. MR imaging of the wrist: comparison between 1.5- and 3-T MR imaging--preliminary experience. *Radiology* 2005, *234*, 256–264.
6. Morakkabati-Spitz, N.; Gieseke, J.; Kuhl, C.; Lutterbey, G.; Falkenhausen, M. von; Traber, F.; Park-Simon, T.-W.; Zivanovic, O.; Schild, H.H. MRI of the pelvis at 3 T: very high spatial resolution with sensitivity encoding and flip-angle sweep technique in clinically acceptable scan time. *Eur Radiol* 2006, *16*, 634–641.
7. Scheidler, J.; Reiser, M.F. MRI of the female and male pelvis: current and future applications of contrast enhancement. *Eur J Radiol* 2000, *34*, 220–228.
8. Leiner, T.; Vries, M. de; Hoogeveen, R.; Vasbinder, G.B.C.; Lemaire, E.; van Engelshoven, J.M.A. Contrast-enhanced peripheral MR angiography at 3.0 Tesla: initial experience with a whole-body scanner in healthy volunteers. *J Magn Reson Imaging* 2003, *17*, 609–614.
9. Willinek, W.A.; Born, M.; Simon, B.; Tschampa, H.J.; Krautmacher, C.; Gieseke, J.; Urbach, H.; Textor, H.J.; Schild, H.H. Time-of-flight MR angiography: comparison of 3.0-T imaging and 1.5-T imaging--initial experience. *Radiology* 2003, *229*, 913–920.
10. Setsompop, K. *Design Algorithms for Parallel Transmission in Magnetic Resonance Imaging*. Doctor of Philosophy; Massachusetts Institute of Technology: Massachusetts Institute of Technology, 2008.
11. Edelstein, W.A.; Glover, G.H.; Hardy, C.J.; Redington, R.W. The intrinsic signal-to-noise ratio in NMR imaging. *Magn Reson Med* 1986, *3*, 604–618.
12. Hoult, D.; Richards, R. The signal-to-noise ratio of the nuclear magnetic resonance experiment. *Journal of Magnetic Resonance* 2011, *213*, 329–343.
13. Hu, X.; Norris, D.G. Advances in high-field magnetic resonance imaging. *Annu Rev Biomed Eng* 2004, *6*, 157–184.

- 14.Ogawa, S.; Lee, T.M.; Nayak, A.S.; Glynn, P. Oxygenation-sensitive contrast in magnetic resonance image of rodent brain at high magnetic fields. *Magn Reson Med* 1990, *14*, 68–78.
- 15.Frayne, R.; Goodyear, B.G.; Dickhoff, P.; Lauzon, M.L.; Sevick, R.J. Magnetic resonance imaging at 3.0 Tesla: challenges and advantages in clinical neurological imaging. *Invest Radiol* 2003, *38*, 385–402.
- 16.Kim, D.-S.; Garwood, M. High-field magnetic resonance techniques for brain research. *Curr Opin Neurobiol* 2003, *13*, 612–619.
- 17.Lin, W.; An, H.; Chen, Y.; Nicholas, P.; Zhai, G.; Gerig, G.; Gilmore, J.; Bullitt, E. Practical consideration for 3T imaging. *Magn Reson Imaging Clin N Am* 2003, *11*, 615-39, vi.
- 18.Scarabino, T.; Nimore, F.; Giannatempo, G.M.; Bertolino, A.; Di Salle, F.; Salvolini, U. 3.0 T magnetic resonance in neuroradiology. *Eur J Radiol* 2003, *48*, 154–164.
- 19.Barth, M.; Metzler, A.; Klarhofer, M.; Roll, S.; Moser, E.; Leibfritz, D. Functional MRI of the human motor cortex using single-shot, multiple gradient-echo spiral imaging. *Magn Reson Imaging* 1999, *17*, 1239–1243.
- 20.Chen, Y.C.; Mandeville, J.B.; Nguyen, T.V.; Talele, A.; Cavagna, F.; Jenkins, B.G. Improved mapping of pharmacologically induced neuronal activation using the IRON technique with superparamagnetic blood pool agents. *J Magn Reson Imaging* 2001, *14*, 517–524.
- 21.Yacoub, E.; Duong, T.Q.; van de Moortele, P.-F.; Lindquist, M.; Adriany, G.; Kim, S.-G.; Ugurbil, K.; Hu, X. Spin-echo fMRI in humans using high spatial resolutions and high magnetic fields. *Magn Reson Med* 2003, *49*, 655–664.
- 22.Bomdorf, H.; Helzel, T.; Kunz, D.; Röschmann, P.; Tschendel, O.; Wieland, J. Spectroscopy and imaging with a 4 tesla whole-body mr system. *NMR Biomed* 1988, *1*, 151–158.
- 23.Collins, C.M.; Liu, W.; Schreiber, W.; Yang, Q.X.; Smith, M.B. Central brightening due to constructive interference with, without, and despite dielectric resonance. *J Magn Reson Imaging* 2005, *21*, 192–196.
- 24.Merkle, E.M.; Dale, B.M. Abdominal MRI at 3.0 T: the basics revisited. *AJR Am J Roentgenol* 2006, *186*, 1524–1532.
- 25.Kuhl, C.K.; Kooijman, H.; Gieseke, J.; Schild, H.H. Effect of B1 inhomogeneity on breast MR imaging at 3.0 T. *Radiology* 2007, *244*, 929–930.
- 26.Glover, G.H.; Hayes, C.E.; Pelc, N.J.; Edelstein, W.A.; Mueller, O.M.; Hart, H.R.; Hardy, C.J.; Donnell, M.O.; Berber, W.D. Comparison of linear and circular polarization for magnetic resonance imaging. *Journal of Magnetic Resonance* 1985, *64*, 255–270.
- 27.Ibrahim, T.S.; Hue, Y.-K.; Tang, L. Understanding and manipulating the RF fields at high field MRI. *NMR Biomed* 2009, *22*, 927–936.
- 28.van de Moortele, P.-F.; Akgun, C.; Adriany, G.; Moeller, S.; Ritter, J.; Collins, C.M.; Smith, M.B.; Vaughan, J.T.; Ugurbil, K. B(1) destructive interferences and spatial phase patterns at 7 T with a head transceiver array coil. *Magn Reson Med* 2005, *54*, 1503–1518.
- 29.Vaughan, J.T.; Garwood, M.; Collins, C.M.; Liu, W.; DelaBarre, L.; Adriany, G.; Andersen, P.; Merkle, H.; Goebel, R.; Smith, M.B.; *et al.* 7T vs. 4T: RF power,

- homogeneity, and signal-to-noise comparison in head images. *Magn Reson Med* 2001, 46, 24–30.
30. Levitt, M.H.; Freeman, R. NMR Population Inversion Using a Composite Pulse. *Journal of Magnetic Resonance* 1979, 473–476.
 31. Saekho, S.; Boada, F.E.; Noll, D.C.; Stenger, V.A. Small tip angle three-dimensional tailored radiofrequency slab-select pulse for reduced B1 inhomogeneity at 3 T. *Magn Reson Med* 2005, 53, 479–484.
 32. Stenger, V.A.; Boada, F.E.; Noll, D.C. Multishot 3D slice-select tailored RF pulses for MRI. *Magn Reson Med* 2002, 48, 157–165.
 33. Tannus, A.; Garwood, M. Adiabatic pulses. *NMR in biomedicine* 1997, 10, 423–434.
 34. Katscher, U.; Bornert, P.; Leussler, C.; van den Brink, J.S. Transmit SENSE. *Magn Reson Med* 2003, 49, 144–150.
 35. Katscher, U.; Bornert, P. Parallel RF transmission in MRI. *NMR Biomed* 2006, 19, 393–400.
 36. Zhu, Y. Parallel excitation with an array of transmit coils. *Magn Reson Med* 2004, 51, 775–784.
 37. Adriany, G.; van de Moortele, P.-F.; Wiesinger, F.; Moeller, S.; Strupp, J.P.; Andersen, P.; Snyder, C.; Zhang, X.; Chen, W.; Pruessmann, K.P.; *et al.* Transmit and receive transmission line arrays for 7 Tesla parallel imaging. *Magn Reson Med* 2005, 53, 434–445.
 38. Metzger, G.J.; Snyder, C.; Akgun, C.; Vaughan, T.; Ugurbil, K.; van de Moortele, P.-F. Local B1+ shimming for prostate imaging with transceiver arrays at 7T based on subject-dependent transmit phase measurements. *Magn Reson Med* 2008, 59, 396–409.
 39. Collins, C.M.; Liu, W.; Swift, B.J.; Smith, M.B. Combination of optimized transmit arrays and some receive array reconstruction methods can yield homogeneous images at very high frequencies. *Magn Reson Med* 2005, 54, 1327–1332.
 40. Ibrahim, T.S.; Lee, R.; Baertlein, B.A.; Abduljalil, A.M.; Zhu, H.; Robitaille, P.M. Effect of RF coil excitation on field inhomogeneity at ultra high fields: a field optimized TEM resonator. *Magn Reson Imaging* 2001, 19, 1339–1347.
 41. Mao, W.; Smith, M.B.; Collins, C.M. Exploring the limits of RF shimming for high-field MRI of the human head. *Magn Reson Med* 2006, 56, 918–922.
 42. Willinek, W.A.; Gieseke, J.; Kukuk, G.M.; Nelles, M.; Konig, R.; Morakkabati-Spitz, N.; Traber, F.; Thomas, D.; Kuhl, C.K.; Schild, H.H. Dual-source parallel radiofrequency excitation body MR imaging compared with standard MR imaging at 3.0 T: initial clinical experience. *Radiology* 2010, 256, 966–975.
 43. Adriany, G.; Auerbach, E.J.; Snyder, C.J.; Gozubuyuk, A.; Moeller, S.; Ritter, J.; van de Moortele, P.-F.; Vaughan, T.; Ugurbil, K. A 32-channel lattice transmission line array for parallel transmit and receive MRI at 7 tesla. *Magn Reson Med* 2010, 63, 1478–1485.
 44. Setsompop, K.; Alagappan, V.; Gagoski, B.; Witzel, T.; Polimeni, J.; Potthast, A.; Hebrank, F.; Fontius, U.; Schmitt, F.; Wald, L.L.; *et al.* Slice-selective RF pulses for in vivo B1+ inhomogeneity mitigation at 7 tesla using parallel RF excitation with a 16-element coil. *Magn Reson Med* 2008, 60, 1422–1432.

45. Vernickel, P.; Roschmann, P.; Findekle, C.; Ludeke, K.-M.; Leussler, C.; Overweg, J.; Katscher, U.; Grasslin, I.; Schunemann, K. Eight-channel transmit/receive body MRI coil at 3T. *Magn Reson Med* 2007, *58*, 381–389.
46. Childs, A.S.; Malik, S.J.; O'Regan, D.P.; Hajnal, J.V. Impact of number of channels on RF shimming at 3T. *MAGMA* 2013, *26*, 401–410.
47. Darji, N.; Kim, K.-N.; Patel, G.; Fautz, H.-P.; Bernarding, J.; Speck, O. Evaluating Further Benefits of B1+ Homogeneity When More Transmit Channels are Used. In *Presented at ISMRM 19th Annual Meeting: Montréal, Québec, Canada, May 2011*.
48. Curtis, A.T.; Gilbert, K.M.; Klassen, L.M.; Gati, J.S.; Menon, R.S. Slice-by-slice B1+ shimming at 7 T. *Magn Reson Med* 2012, *68*, 1109–1116.
49. Snyder, C.J.; DelaBarre, L.; Moeller, S.; Tian, J.; Akgun, C.; van de Moortele, P.-F.; Bolan, P.J.; Ugurbil, K.; Vaughan, J.T.; Metzger, G.J. Comparison between eight- and sixteen-channel TEM transceive arrays for body imaging at 7 T. *Magn Reson Med* 2012, *67*, 954–964.
50. Van de Moortele, P.-F.; Akgun, C.; Snyder, C.; DelaBarre, L.; Adriany, G.; Vaughan, T.; Ugurbil, K. Impact of Coil Diameter and Number of Coil Elements on B1 Destructive Interferences with Stripline Coil Arrays at 7 Tesla. In *Presented at ISMRM 14th Annual Meeting: Seattle, Washington, USA, May 2006*.
51. Wu, X.; Sebastian, S.; Adriany, G.; Auerbach, E.; Ugurbil, K.; van de Moortele, P.-F. Enhanced Whole Brain Excitation Performance of Parallel Transmission with a Z- Encoding RF Coil Array at 7T. In *Presented at ISMRM 20th Annual Meeting: Melbourne, Victoria, Australia, May 2012*.
52. Nishimura, D. *Principles of Magnetic Resonance Imaging*, 1995.
53. Zhi-Pei, L.; Lauterbur, P.C. *Principles of Magnetic Resonance Imaging: A Signal Processing Perspective*; Wiley-IEEE Press, 1999.
54. Saekho, S. *B1+ inhomogeneity compensation in magnetic resonance imaging (MRI)*, 2004.
55. A N Garroway, P.K.G.M. Image formation in NMR by a selective irradiative process. *Journal of Physics C: Solid State Physics* 2001, *7*, L457.
56. Griffiths, D.J. *Introduction to Electrodynamics, ed. Second.*: New Jersey: Prentice Hall., 1989,
57. Alecci, M.; Collins, C.M.; Smith, M.B.; Jezzard, P. Radio frequency magnetic field mapping of a 3 Tesla birdcage coil: experimental and theoretical dependence on sample properties. *Magn Reson Med* 2001, *46*, 379–385.
58. Yang, Q.X.; Wang, J.; Zhang, X.; Collins, C.M.; Smith, M.B.; Liu, H.; Zhu, X.-H.; Vaughan, J.T.; Ugurbil, K.; Chen, W. Analysis of wave behavior in lossy dielectric samples at high field. *Magn Reson Med* 2002, *47*, 982–989.
59. Ibrahim, T.S.; Lee, R.; Abduljalil, A.M.; Baertlein, B.A.; Robitaille, P.M. Dielectric resonances and B(1) field inhomogeneity in UHFMRI: computational analysis and experimental findings. *Magn Reson Imaging* 2001, *19*, 219–226.
60. Bloch, F. Nuclear Induction. *Phys Rev* 1946, 460–474.
61. Pauly, J.M.; Nishimura, D.G.; Macovski, A. Introduction to: A k-space analysis of small-tip-angle excitation. *J Magn Reson* 2011, *213*, 558–559.
62. Ullmann, P.; Junge, S.; Wick, M.; Seifert, F.; Ruhm, W.; Hennig, J. Experimental analysis of parallel excitation using dedicated coil setups and simultaneous RF transmission on multiple channels. *Magn Reson Med* 2005, *54*, 994–1001.

63. Akoka, S.; Franconi, F.; Seguin, F.; Le Pape, A. Radiofrequency map of an NMR coil by imaging. *Magn Reson Imaging* 1993, *11*, 437–441.
64. Griswold, M.; Kannengiesser, S.; Muller, M.; Jakob, P. Autocalibrated accelerated parallel excitation (transmit-GRAPPA). In *Presented at ISMRM 13th Annual Meeting*: Miami Beach, FL, USA, May 2005.
65. Griswold, M.A.; Jakob, P.M.; Heidemann, R.M.; Nittka, M.; Jellus, V.; Wang, J.; Kiefer, B.; Haase, A. Generalized autocalibrating partially parallel acquisitions (GRAPPA). *Magn Reson Med* 2002, *47*, 1202–1210.
66. Grissom, W.; Yip, C.-y.; Zhang, Z.; Stenger, V.A.; Fessler, J.A.; Noll, D.C. Spatial domain method for the design of RF pulses in multicoil parallel excitation. *Magn Reson Med* 2006, *56*, 620–629.
67. Pruessmann, K.P.; Weiger, M.; Scheidegger, M.B.; Boesiger, P. SENSE: sensitivity encoding for fast MRI. *Magn Reson Med* 1999, *42*, 952–962.
68. Barker, G.J.; Simmons, A.; Arridge, S.R.; Tofts, P.S. A simple method for investigating the effects of non-uniformity of radiofrequency transmission and radiofrequency reception in MRI. *Br J Radiol* 1998, *71*, 59–67.
69. John, P.; Dwight, N.; Albert, M. A linear class of large-tip-angle selective excitation pulses. *Journal of Magnetic Resonance (1969)* 1989, 571–587.
70. Saekho, S.; Yip, C.-y.; Noll, D.C.; Boada, F.E.; Stenger, V.A. Fast-kz three-dimensional tailored radiofrequency pulse for reduced B1 inhomogeneity. *Magn Reson Med* 2006, *55*, 719–724.
71. Yip, C.-y.; Fessler, J.A.; Noll, D.C. Advanced three-dimensional tailored RF pulse for signal recovery in T2*-weighted functional magnetic resonance imaging. *Magn Reson Med* 2006, *56*, 1050–1059.
72. Zelinski, A.C.; Wald, L.L.; Setsompop, K.; Goyal, V.K.; Adalsteinsson, E. Sparsity-enforced slice-selective MRI RF excitation pulse design. *IEEE Trans Med Imaging* 2008, *27*, 1213–1229.
73. Ma, C.; Xu, D.; King, K.F.; Liang, Z.-P. Joint design of spoke trajectories and RF pulses for parallel excitation. *Magn Reson Med* 2011, *65*, 973–985.
74. Jankiewicz, M.; Zeng, H.; Moore, J.E.; Anderson, A.W.; Avison, M.J.; Welch, E.B.; Gore, J.C. Practical considerations for the design of sparse-spokes pulses. *J Magn Reson* 2010, *203*, 294–304.
75. Christ, A.; Kainz, W.; Hahn, E.G.; Honegger, K.; Zefferer, M.; Neufeld, E.; Rascher, W.; Janka, R.; Bautz, W.; Chen, J.; *et al.* The Virtual Family--development of surface-based anatomical models of two adults and two children for dosimetric simulations. *Phys Med Biol* 2010, *55*, N23-38.
76. Collins, C.; Wang, Z.; Smith, M. A Conservative Method for Ensuring Safety within Transmit Arrays. In *Presented at ISMRM 15th Annual Meeting*: Berlin, Germany, May 2007.
77. Klose, U. Mapping of the radio frequency magnetic field with a MR snapshot FLASH technique. *Med Phys* 1992, *19*, 1099–1104.
78. Fautz, H.-P.; Vogel, M.; Gross, P.; Kerr, A.; Zhu, Y. B1 Mapping of Coil Arrays for Parallel Transmission. In *Presented at ISMRM 16th Annual Meeting*: Toronto, Ontario, Canada, May 2008.

79. Setsompop, K.; Wald, L.L.; Alagappan, V.; Gagoski, B.A.; Adalsteinsson, E. Magnitude least squares optimization for parallel radio frequency excitation design demonstrated at 7 Tesla with eight channels. *Magn Reson Med* 2008, 59, 908–915.
80. Pinkerton, R.G.; McKinnon, G.C.; Menon, R.S. SENSE optimization of a transceive surface coil array for MRI at 4 T. *Magn Reson Med* 2006, 56, 630–636.
81. Schneider, J.T.; Kalayciyan, R.; Haas, M.; Herrmann, S.R.; Ruhm, W.; Hennig, J.; Ullmann, P. Inner-volume imaging in vivo using three-dimensional parallel spatially selective excitation. *Magn Reson Med* 2013, 69, 1367–1378.
82. Brinkmann, I.; Darji, N.; Speck, O.; Bock, M. BOLD MRI of the Kidneys under water loading at 7 Tesla using parallel Transmission and RF Shimming of individual. In *Presented at ISMRM 22th Annual Meeting: Milan, Italy, May 2014*, p. 1009.
83. Darji, N.; Haas, M.; Patel, G.; Speck, O.; Brinkmann, I.; Bock, M. Imaging the Kidneys at 7T Using 8Tx/32Rx Abdominal Coil and RF Shimming of Individual Slices. In *Presented at ISMRM 21th Annual Meeting: Salt Lake City, Utah, USA, April 2013*.
84. Homann, H.; Graesslin, I.; Nehrke, K.; Findekle, C.; Dossel, O.; Bornert, P. Specific absorption rate reduction in parallel transmission by k-space adaptive radiofrequency pulse design. *Magn Reson Med* 2011, 65, 350–357.
85. Gilbert, K.M.; Belliveau, J.-G.; Curtis, A.T.; Gati, J.S.; Klassen, L.M.; Menon, R.S. A conformal transceive array for 7 T neuroimaging. *Magn Reson Med* 2012, 67, 1487–1496.

Publications

Journal Articles

- **Darji N.**, Patel G. and Speck O.; Gain of Imaging Fidelity by Employing Higher Number of Independent Transmit channel Together with Slice-Selective RF shimming at 7T, *Materials*, 2014. 7(1), 30-43

Conference Publications

- Brinkmann, I.; **Darji, N.**; Speck, O.; Bock, M. BOLD MRI of the Kidneys under water loading at 7 Tesla using parallel Transmission and RF Shimming of individual. In *ISMRM*, 2014, p. 1009. (Electronic poster)
- **Darji N.**, Haas M., Patel G., Speck O., I. Brickmann and Bock M.. Imaging the kidney at 7T using 8Tx/32Rx Abdominal coil and RF shimming of individual slice, *ISMRM*. Salt Lake City, USA, 2013. (Electronic poster).
- **Darji N.**, Kim K.-N., Patel G., Fautz H.-P., Bernarding J., and Speck O.. Evaluating Further Benefits of B1+ Homogeneity When More Transmit Channels Are Used, *ISMRM*. Montreal, Canada, May, 2011. (Oral presentation).
- Kim K.- N., **Darji N.**, Herrmann T., Mallow J., Cho Z.-H., Speck O. and Bernarding J.. Improved B1+ Field using a 16-Channel Transmit Head Array & an 8 Channel PTx System at 7T, *ISMRM*, Montreal, 2011. (Electronic poster).
- Danishad K. A., **Darji N.** and Speck O.. Further Reduction of SAR For T2- Weighted Hyper-TSE Imaging At 7 Tesla. *ISMRM*, Montreal, 2011. (Oral presentation).
- **Darji N.**, Patel G., Fautz H-P. and Speck O.. Multi slice shimming approach using pTx at high field. *ESMRMB*. Leipzig, Germany 2011. (Oral presentation).
- **Darji N.**, Ramm M., and Speck O.. Basis for Contrast Enhanced T1- Weighted Imaging Using SE at High Field. *ISMRM*, Stockholm, May, 2010. (Poster presentation).

Erklärung

Hiermit erkläre ich, dass ich die von mir eingereichte Dissertation zum dem Thema

“Efficiency of Parallel Transmission Methods at 7T Magnetic Resonance”

selbständig verfasst, nicht schon als Dissertation verwendet habe und die benutzten Hilfsmittel und Quellen vollständig angegeben wurden.

Weiterhin erkläre ich, dass ich weder diese noch eine andere Arbeit zur Erlangung des akademischen Grades doctor rerum naturalium (Dr. rer. nat.) an einer anderen Einrichtungen eingereicht habe.

Magdeburg, 10.06.2014

Unterschrift